iScience

CellPress

Article

Srsf7 Establishes the Juvenile Transcriptome through Age-Dependent Alternative Splicing in Mice

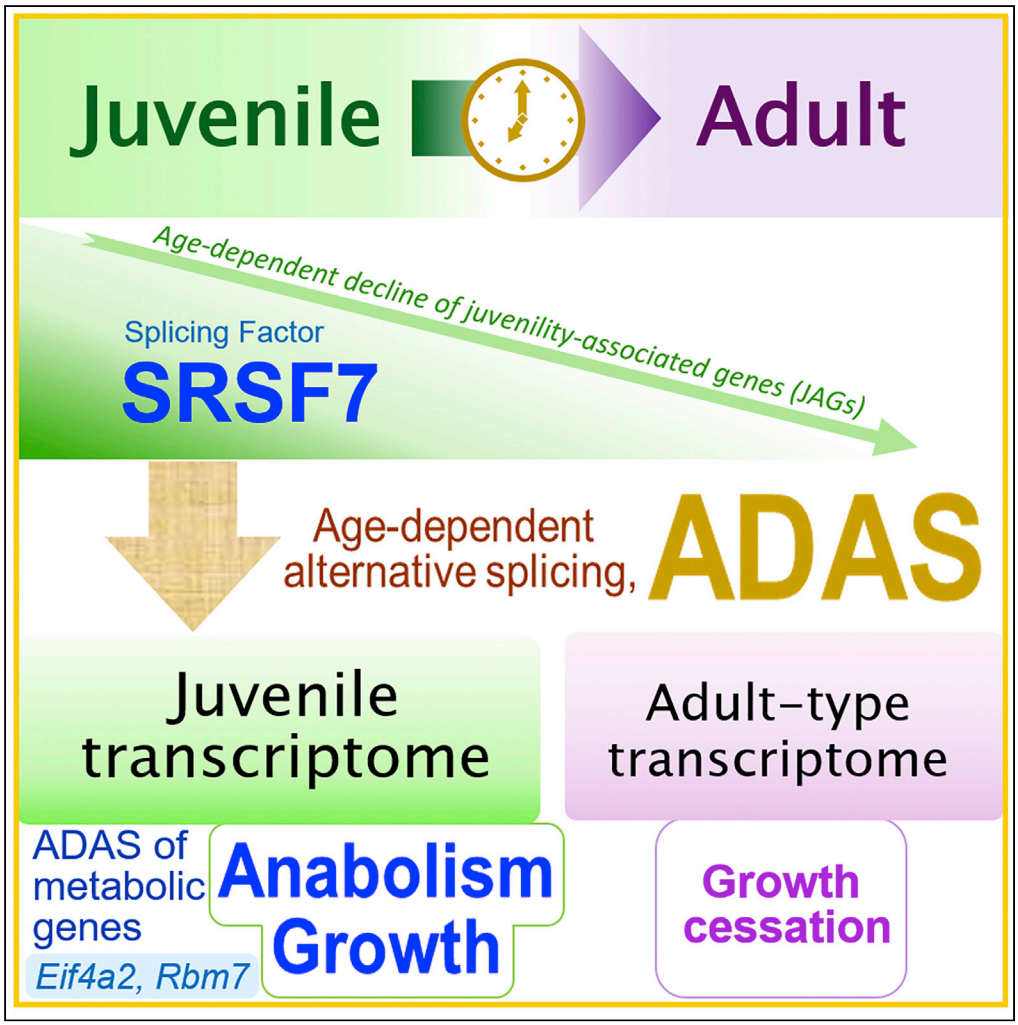

Yosuke Kadota, Faidruz Azura Jam, Haruka Yukiue, ..., Mayu Fukumura, Ikuo Tooyama, Masaki Mori

morim@belle.shiga-med.ac.jp

HIGHLIGHTS

Age-dependent alternative splicing (ADAS) was determined in mice

Srsf7 depletion causes loss of cellular juvenescence

Srsf7 mutation causes a shift from juvenile to adult-type transcriptome

Srsf7 promotes juvenile growth and anabolism through ADAS

Kadota et al., iScience *23*, 100929
March 27, 2020
https://doi.org/10.1016/j.isci.2020.100929

iScience

CellPress

Article

Srsf7 Establishes the Juvenile Transcriptome through Age-Dependent Alternative Splicing in Mice

Yosuke Kadota,[1,4] Faidruz Azura Jam,[1,4] Haruka Yukiue,[1,4] Ichiro Terakado,[2] Takao Morimune,[1,3] Ayami Tano,[1] Yuya Tanaka,[1] Sayumi Akahane,[1] Mayu Fukumura,[1] Ikuo Tooyama,[1] and Masaki Mori[1,5,*]

SUMMARY

The juvenile phase is characterized by continuously progressing physiological processes such as growth and maturation, which are accompanied by transitions in gene expression. The contribution of transcriptome dynamics to the establishment of juvenile properties remains unclear. Here, we investigated alternative splicing (AS) events in postnatal growth and elucidated the landscape of age-dependent alternative splicing (ADAS) in C57BL/6 mice. Our analysis of ADAS in the cerebral cortex, cardiomyocytes, and hepatocytes revealed numerous juvenile-specific splicing isoforms that shape the juvenile transcriptome, which in turn functions as a basis for the highly anabolic status of juvenile cells. Mechanistically, the juvenile-expressed splicing factor Srsf7 mediates ADAS, as exemplified by switching from juvenile to adult forms of anabolism-associated genes *Eif4a2* and *Rbm7*. Suppression of Srsf7 results in "fast-forwarding" of this transcriptome transition, causing impaired anabolism and growth in mice. Thus, juvenile-specific AS is indispensable for the anabolic state of juveniles and differentiates juveniles from adults.

INTRODUCTION

Organisms undergo age-dependent alterations in body size and function as they grow into adults. One of the mechanisms regulating this process is an age-dependent transition in gene expression that is regulated at the transcriptional and post-transcriptional levels. Transcription is a process of mRNA synthesis controlled quantitatively by factors such as RNA polymerases, transcription factors, and chromatin modifiers. Transcription is also controlled qualitatively by the use of alternative transcription start sites and alternative polyadenylation. The post-transcriptional processing includes alternative splicing (AS), (de)stabilization, RNA modifications such as RNA methylation (Zhao et al., 2016), RNA editing, interaction with RNA-binding protein (RBP, Anders et al., 2012) and microRNA, transportation, and compartmentalization.

AS increases transcript diversity. Following the discovery of splicing (Berget et al., 1977; Chow et al., 1977), AS was identified as a system that generated multiple variant mRNAs from one gene (Alt et al., 1980; Early et al., 1980). This process enables a limited number of genes to generate more molecules. AS thus expands the proteome (Nilsen and Graveley, 2010) and is relevant to evolution (Barbosa-Morais et al., 2012). AS occurs in tissue-specific patterns (Blekhman et al., 2010; Ellis et al., 2012) and cell-type-specific patterns (e.g., embryonic stem cells [Han et al., 2013; Salomonis et al., 2010]), suggesting its role in differentiating cellular contexts. AS has broad biological implications in synapse formation (Ule et al., 2005), sex determination (Baker, 1989), the epithelial-mesenchymal transition (Warzecha et al., 2009), etc. AS is also implicated in pathogenesis (Cieply and Carstens, 2015; Tazi et al., 2009) and cancer (Venables et al., 2009). Despite the multifaceted nature of AS, its age dependency is not well understood. Here, we investigate age-dependent alternative splicing (ADAS) in the context of postnatal organ growth in mice.

The postnatal growth phase is a process in which an animal incorporates nutrition for anabolism, thus growing in size. In addition, the functions of the organs mature during the process of growing into an adult. For example, the brain undergoes striking functional enhancement via functional plasticity (Hensch, 2005). Thus, juvenile animals possess distinct physiological characteristics, which we call "juvenile properties" (Jam et al., 2018; Tano et al., 2019). Despite its particular physiological traits, the juvenile phase has not been studied as rigorously as the fetal development or adult phases. Thus, to explore these juvenile

[1]Molecular Neuroscience Research Center (MNRC), Shiga University of Medical Science, Seta Tsukinowa-cho, Otsu, Shiga 520-2192, Japan

[2]Research Center for Animal Life Science (RCALS), Shiga University of Medical Science, Seta Tsukinowa-cho, Otsu, Shiga 520-2192, Japan

[3]Department of Pediatrics, Shiga University of Medical Science, Seta Tsukinowa-cho, Otsu, Shiga 520-2192, Japan

[4]These authors contributed equally

[5]Lead Contact

*Correspondence: morim@belle.shiga-med.ac.jp

https://doi.org/10.1016/j.isci.2020.100929

properties, we previously performed a comprehensive transcriptome analysis in mice of different ages and identified juvenility-associated genes (JAGs, Jam et al., 2018) and juvenility-associated long noncoding RNAs (JALNCs, Tano et al., 2019) as molecular building blocks of juvenile properties. These analyses revealed that the juvenile phase is characterized by a specific gene expression profile (hereafter, juvenile transcriptome) quite distinct from that of adults.

Our analyses of the juvenile transcriptome identified AS as an important mechanism regulating juvenile properties (Jam et al., 2018), although the details remained unaddressed. Here, we show that juveniles undergo global AS in an age-dependent manner that shapes the juvenile transcriptome. AS is the differential removal of introns from pre-mRNA and is observed in 92%–94% of multi-exon genes (Pan et al., 2008; Wang et al., 2008). Splicing is carried out in spliceosomes that consist of five small nuclear ribonucleoprotein particles (snRNPs), U1, U2, U4/U6, and U5; these snRNPs are the major components of the spliceosome, and numerous auxiliary proteins are also present (Chen and Manley, 2009). Spliceosome assembly is a highly dynamic process that starts with the binding of SR proteins to exonic splicing enhancer (ESE); these proteins stabilize the interaction of the U1 snRNP to the 5′ splicing site (5′ ss) of the intron via base pairing with snRNA1 (Long and Caceres, 2009). The SR proteins also recruit the U2AF complex and U2 snRNP to the 3′ ss (Chen and Manley, 2009; Nilsen and Graveley, 2010). Further incorporation of the U4/U6–U5 tri-snRNP leads to the formation of a complex that contains all subunits, followed by extensive conformational changes, resulting in the formation of the catalytically active spliceosome.

The Srsf7 splicing factor belongs to the SR protein family, which is encoded by nine genes in humans: *SRSF1* (chr17), *SRSF2* (chr17), *SRSF3* (chr6), *SRSF4* (chr1), *SRSF5* (chr14), *SRSF6* (chr20), *SRSF7* (chr2), *SRSF9* (chr12), *SRSF11* (chr1, Shepard and Hertel, 2009). The SR splicing factors possess an N-terminal RNA-binding domain (RBD) and a C-terminal RS domain that is enriched with arginine-serine dipeptides. The RS domain mediates protein-protein interactions that are required for spliceosome assembly (Kohtz et al., 1994; Wu and Maniatis, 1993). Srsf7 additionally possesses a zinc-affinity domain between the RBD and the RS domain (Jeong, 2017). It was also reported that a binding location relative to the 5′ ss affects the splicing regulation function of Srsf7 (Erkelenz et al., 2013). Srsf7 transports herpes simplex virus 1 mRNAs (Escudero-Paunetto et al., 2010) and is involved in processing HIV-1 mRNA (Valente et al., 2009), but the biological roles of Srsf7 remain largely unknown.

Here, we describe ADAS in postnatally growing mouse organs as a model and investigate a role for Srsf7 in the regulation of ADAS. Our analysis provides a landscape for ADAS and clarifies a role for Srsf7 in ADAS and the establishment of the juvenile transcriptome.

RESULTS

Age-Dependent Alternative Splicing in Growing Organ Transcriptomes

To comprehensively address ADAS, we performed a transcriptome analysis with mouse organs and analyzed AS events in a transcriptome-wide manner. We performed RNA sequencing (RNA-seq) analysis with the cerebral cortex (CC) of C57BL/6N mice in the juvenile and adult phases. We utilized postnatal day 1 (P1) and P14 as juvenile phases and P56 as an adult phase. We combined the data from the CC with our previously publicized dataset of cardiomyocytes (CMs) and hepatocytes (Heps) from mice of juvenile (P1 and P7) and adult (P56) phases (Jam et al., 2018). We investigated AS events among the different ages using the mixture-of-isoforms (MISO) model (Katz et al., 2010) and comprehensively identified AS events that occurred in a phase-specific manner as ADAS events (Figure 1A). This analysis identified numerous ADAS events, as examples, in *Tpm2*, *Ndrg2*, and *Fn1* (Figure 1B). *Tpm2* underwent exon skipping in which an exon was included in a juvenile-specific manner (juvenile-exon inclusion). In contrast, *Ndrg2* underwent exon skipping in an adult-specific manner. *Fn1* underwent multiple AS events that consisted of mutually exclusive exon usage, with distinct juvenile and adult exon inclusions.

The analysis of AS events identified 1,264, 408 and 371 total ADAS events in the CC, CMs, and Heps, respectively (Figure 1C). Among the five types of ADAS (exon skipping, intron retention, mutually exclusive exons, 5′ or 3′ alternative ss), exon skipping was the most frequent (Figure 1D). There were two types of exon skipping: juvenile- and adult-enriched exon inclusion. Adult-enriched exon inclusion was more frequent (533 events) than juvenile-enriched exon inclusion (238 events, Figure 1E). To determine the biological relevance of ADAS, a Gene Ontology (GO) analysis was performed for the differentially spliced genes at the juvenile and adult phases ("ADAS-target genes"). The ADAS-target genes were significantly

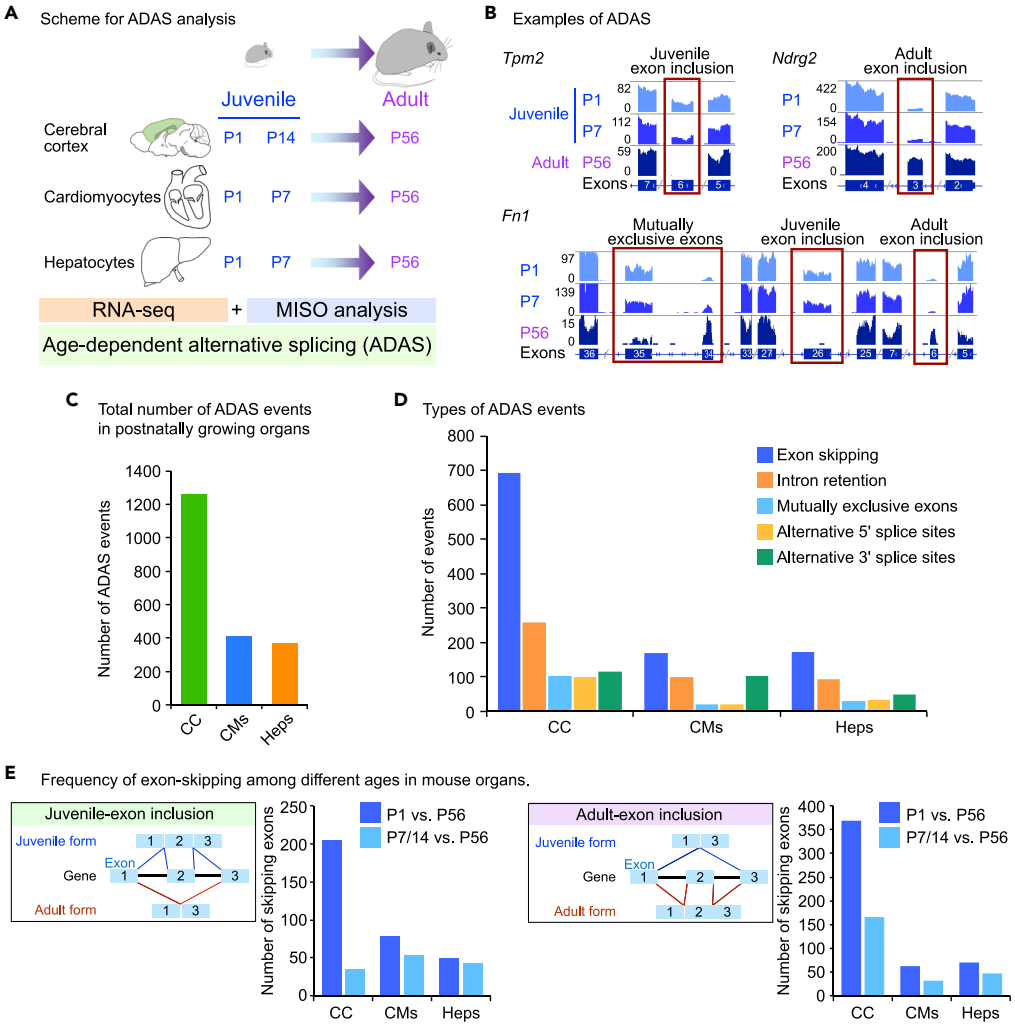

Figure 1. Comprehensive Identification of Age-Dependent Alternative Splicing (ADAS) in Organ Growth

(A) Schematic of the age-dependent alternative splicing (ADAS) analysis in this study. MISO, mixture of isoforms.

(B) Representative examples of ADAS events in postnatal cardiomyocytes. Numbers shown to the left of the read patterns indicate FPKM values. Exon information was shown below.

(C) Total number of ADAS events in cerebral cortex (CC), cardiomyocytes (CMs), and hepatocytes (Heps). The alternative splicing (AS) events were analyzed by MISO, and AS events with Bayes factors > $10^{1/2}$ were counted.

(D) Numbers of each AS pattern in postnatally growing mouse organs.

(E) Frequency of juvenile- or adult-enriched specific exon inclusions. The frequency was compared between P1 and P56 or between P7 (CMs and Heps)/P14 (CC) and P56.

See also Figure S1.

associated with "nervous system development" and "axonogenesis" in the CC, "cell-cell adhesion" and "muscle contraction" in CMs, and "mitochondrial fission" and "extracellular exosome" in Heps. These results indicate that the ADAS-target genes are engaged in the biologically relevant functions (Figure S1). Thus, we comprehensively determined the ADAS events in postnatal growth and identified the juvenile-specific splicing isoforms.

Juvenile Expression of *Srsf7*

We next explored how the ADAS events were regulated. We hypothesized that juvenile-specific AS was mediated by juvenile-specifically expressed splicing factor(s) (SFs), so we tested whether SFs were expressed in a juvenile-specific manner. We investigated 59 SFs that were curated manually (Giulietti et al., 2013). Unexpectedly, most of the SF genes were expressed more highly in juvenile tissues throughout

the CC, CMs, and Heps, suggesting their functional relevance in juveniles (Figure S2). Among the juvenile-expressed SFs, we narrowed down the candidate genes for functional analyses by choosing those with robust and at least 2-fold higher expression than in adult in the three tissues. Among the seven genes, *Ybx1*, *hnRNP A0*, *hnRNP A1*, *hnRNP DL*, *Sfpq*, *Srsf2*, and *Srsf7*, we focused on *Srsf7* with a relatively unknown biological function. We will analyze the remaining six genes in a future work. *Srsf7* exhibited prominent juvenile-specific expression with high expression levels in juveniles in all three cell types (Figure 2A). This juvenile-predominant expression was validated with quantitative PCR (Figure 2B). Our previous analysis revealed that Srsf7 was suppressed in cellular juvenescence loss induced by depletion of the JALNC *Gm14230* (Tano et al., 2019). Immunocytochemistry revealed that Srsf7 was localized predominantly to the nucleoplasm in Neuro2a mouse neuroblastoma cells at a lower cell density (Figures 2C and 2D). At a higher cell density, Srsf7 expression was suppressed (Figures 2C and 2D). This cell-density-dependent expression suggests a role for Srsf7 in the regulation of cellular growth.

We next asked whether Srsf7 expression depends on cellular juvenescence. Zeocin, a genotoxic agent, induces loss of cellular juvenescence in NIH3T3 cells (Tano et al., 2019). We applied this method to Neuro2a cells and observed highly efficient induction of cellular senescence, as indicated by senescence-associated β-galactosidase (SA-β-gal) activity and extension of the cytoplasm (Serrano et al., 1997) (Figures 2E and 2F). Srsf7 expression was significantly suppressed in the senescent cells (Figures 2G and 2H), and this result was corroborated by western blot analysis (Figures 2I and S2B). We also analyzed the juvenescence-dependent expression of Srsf7 in another model for cellular senescence. Cellular senescence can be induced by oncogenic genes such as *Ras* (Serrano et al., 1997), *BRAF* (Wajapeyee et al., 2008), *Akt* (Chen et al., 2005), and *E2F* (Denchi et al., 2005). The forced expression of *RasV12* by doxycycline-inducible manner provoked cellular senescence, which was evidenced by changes in cell morphology and impaired cell growth (Figures S2C). The *RasV12*-induced cellular senescence was accompanied by suppression of Srsf7 and enhancement of proteins associated with cellular senescence (Figures S2C–S2E). Thus, *Srsf7* is more highly expressed in juvenile organs and juvenescent cells.

Depletion of *Srsf7* Causes Loss of Cellular Juvenescence and Metabolic Dysfunction

To study the role of *Srsf7* in cellular juvenescence, we tested the influence of *Srsf7* depletion in Neuro2a cells. siRNA-mediated knockdown of *Srsf7* (Figure 3A) significantly suppressed cell growth (Figures 3B and 3C), indicating that *Srsf7* was essential for cell growth. The *Srsf7*-depleted cells were refractory to retinoic acid-induced neural differentiation, indicating that the *Srsf7*-depleted cells lost their ability to differentiate (Figure 3D). The earlier findings that Srsf7 was expressed in juvenile cells prompted us to test whether Srsf7 is required for cellular juvenescence. Srsf7 knockdown led to a profound increase in positive staining in an SA-β-gal assay (Figures 3E and 3F) and the expression of the senescence-associated proteins p16, p27, and γH2ax (Figures 3G and S3A). These results indicate that Srsf7 is essential for cellular juvenescence. We next assessed a role for Srsf7 in counteracting the cellular senescence. The Neuro2a-RasV12 cells were transfected with *Srsf7* or control empty plasmid, followed by doxycycline treatment to induce the cellular senescence. The forced expression of *Srsf7* suppressed the morphological changes of the cells, in comparison with the control plasmid-transfected cells (Figures S3B and S3C).

To analyze the mechanism of growth regulation by *Srsf7*, we assessed the expression of metabolism-associated proteins. *Srsf7* depletion caused decreased phosphorylation of the ribosomal protein S6 (Ser240/244), suggesting impaired protein synthesis (Figure 3G). Additionally, *Srsf7* knockdown induced form II of Lc3, a hallmark of autophagy, suggesting that *Srsf7* depletion caused energy starvation. The findings implied that Srsf7 is required for cell anabolism. To assess the metabolic function of Srsf7, we measured cellular metabolism with a flux analyzer and revealed that *Srsf7* depletion led to a decreased oxygen consumption rate (OCR, Figure 3H) with minor effects on extracellular acidification rate (ECAR Figure 3I), suggesting that mitochondrial function was impaired. Analysis of the OCR to ECAR ratio showed *Srsf7* depletion compromised oxidative phosphorylation (Figure 3J), causing a shift to glycolysis (Figure 3K). We next addressed how the *Srsf7* depletion led to the metabolic shift toward the compromised oxidative phosphorylation. We first assessed mitochondrial quantity by measuring the amount of mitochondrial genome DNA. This analysis did not show a significant change in the mitochondrial quantity upon *Srsf7* depletion (Figure S3D). The expression of mitochondrial protein Cox1 did not alter apparently (Figure 3G). To investigate the potential mechanism behind the metabolic shift, we established *Srsf7*-knockout (KO) Neuro2a cell lines via CRISPR technology and performed transcriptome analysis. The RNA-seq analysis revealed upregulation of *pyruvate dehydrogenase kinase* (*Pdk1*) and *Pdk2* in the *Srsf7*-KO cells. These findings were validated via qPCR (Figure S3E). Pdk proteins direct the metabolic flow from the oxidative phosphorylation to

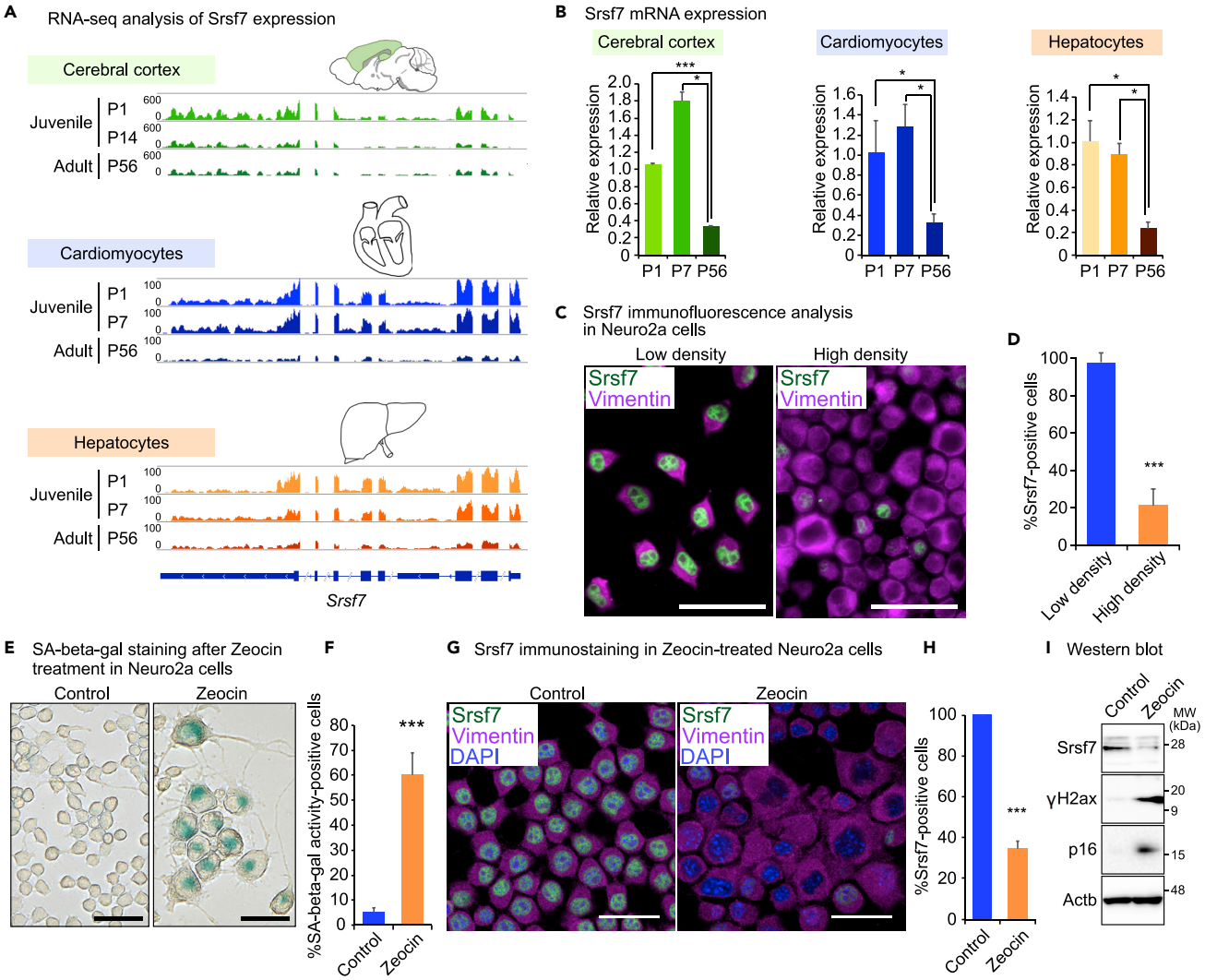

Figure 2. *Srsf7* Is Expressed in Juvenile Organs and Juvenescent Cells

(A) IGV views of *Srsf7* expression in the cerebral cortex (CC), cardiomyocytes (CMs), and hepatocytes (Heps) at juvenile phase postnatal day 1 (P1), P7 (CMs and Heps), or P14 (CC) and adult phase P56. Numbers next to the read patterns (0, 100, and 600) indicate FPKM values.

(B) qPCR analysis of *Srsf7* mRNA expression in CC, CMs, and Heps. Data were normalized to *Polr2a*.

(C) Immunofluorescent analysis of Srsf7 and Vimentin in Neuro2a cells at low and high densities. Scale bar, 50 μm.

(D) Frequency of Srsf7-expressing cells among total cells. *** $p < 0.001$. *n* = 266 and 243 cells. Data are the means ± standard deviations from three independent experiments.

(E) Staining of senescence-associated β-galactosidase (SA-β-gal) activity in cells treated with zeocin at 80 μg/mL for 96 h. Scale bar, 50 μm.

(F) Frequency of cells positive for SA-β-gal staining. *** $p < 0.001$. *n* = 365 and 158 cells. Data are the means ± standard deviations from three independent experiments.

(G) Immunofluorescent analysis of Srsf7 in Neuro2a cells with or without zeocin treatment. Scale bar, 50 μm.

(H) Frequency of Srsf7-expressing cells among total cells. *** $p < 0.001$. *n* = 465 and 291 cells. Data are the means ± standard deviations from three independent experiments.

(I) Western blot analysis with Neuro2a cells treated with zeocin. The senescence marker proteins γH2ax and p16 were increased in zeocin-treated cells. Actb was used as a loading control.

*$p < 0.05$ and ***$p < 0.001$, Student's t test. Data are represented as the means ± standard deviations. See also Figure S2.

glycolysis (Kim et al., 2006; Kluza et al., 2012; Kon et al., 2017). The enhancement of Pdk1 was also observed at the protein level in the cells depleted for *Srsf7* (Figure 3G). Together, *Srsf7* depletion causes the glycolysis-predominant state that is accompanied with the upregulation of Pdk. Thus, *Srsf7* is essential for cellular juvenescence and mediates cellular anabolism.

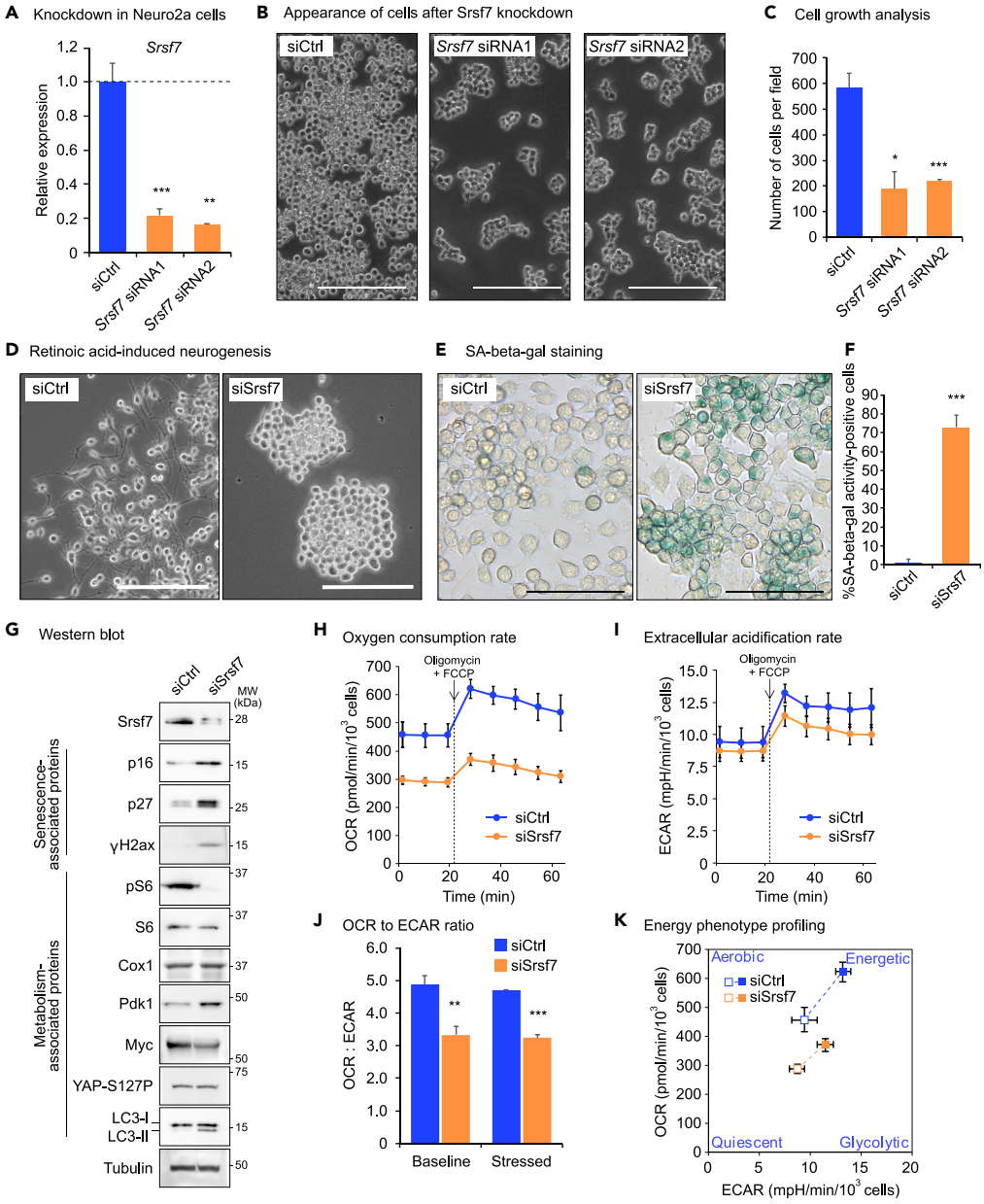

Figure 3. *Srsf7* Is Essential for Cellular Juvenescence

(A) *Srsf7* knockdown efficiency was analyzed by qPCR of *Srsf7* in Neuro2a cells 48 h after transfection with control siRNA or *Srsf7* siRNA. Data were normalized to *Actb*.

(B) Appearance of Neuro2a cells 72 h after transfection with control siRNA or *Srsf7* siRNA. Scale bar, 100 μm.

(C) Number of cells per field 72 h after transfection with control siRNA or *Srsf7* siRNA.

(D) Appearance of Neuro2a cells treated with 20 μM retinoic acid for 48 h to induce neural differentiation. *Srsf7*-depleted cells were refractory to differentiation induction. Scale bar, 100 μm.

(E) Staining of senescence-associated β-galactosidase (SA-β-gal) activity in Neuro2a cells 72 h after transfection with control siRNA or *Srsf7* siRNA. Scale bar, 100 μm.

(F) Frequency of cells positive for SA-β-gal staining among total cells. *** $p < 0.001$. $n = 147$ and 184 cells. Data are the means ± standard deviations from three independent experiments.

(G) Western blot analysis with Neuro2 cells 72 h after transfection of control siRNA or *Srsf7* siRNA. The senescence marker proteins p16, p27, and γH2ax were increased in *Srsf7*-depleted cells. Tubulin was used as a loading control.

(H–K) Analysis of cell metabolism with a flux analyzer in Neuro2a cells 48 h after transfection of control siRNA or *Srsf7* siRNA. (H) Oxygen consumption rate (OCR) and (I) extracellular acidification rate (ECAR) were measured at baseline and

Figure 3. *Continued*

under stress conditions in which cells were treated with oligomycin and FCCP. (J) OCR to ECAR ratio at the baseline and stress conditions. (K) Energy phenotype profile of the cells transfected with control siRNA or *Srsf7* siRNA.
* $p < 0.05$, ** $p < 0.01$, and *** $p < 0.001$, Student's t test. Data are represented as the means ± standard deviations. See also Figure S3.

Srsf7 Regulates Growth and JAGs in Mice

To assess the role of Srsf7 in ADAS in mice, we sought to analyze *Srsf7*-knockout (KO) mice. Using CRISPR-Cas9 genome editing (Cong et al., 2013; Inui et al., 2015; Mali et al., 2013), we designed a guide RNA that introduced a double-strand break in the proximal region downstream of the initiating codon in *Srsf7* (Figure S4A). This break resulted in an indel that caused a frameshift (fs) mutation (Figure S4B). Analysis of newborns revealed that none had homozygous mutations, implying that the null mutation caused embryonic lethality. Analysis of fetuses at embryonic day 7.5 (E7.5) revealed that 18 fetuses (27.6%) were wild-type (WT, $Srsf7^{WT/WT}$), 30 (46.1%) were heterozygous mutants ($Srsf7^{WT/fs}$), and 17 (26.1%) were absorbed embryos, hampering the determination of a genotype (Figure S4C). The absence of a viable homozygous mutant at E7.5 suggested early embryonic lethality. KO of *Srsf3* (also known as SRp20), a gene that encodes the SF with the closest similarity to Srsf7 (Blanco and Bernabéu, 2012; Cavaloc et al., 1999), causes developmental failure at the blastocyst stage (Jumaa et al., 1999). We therefore analyzed whether *Srsf7*-null embryos had defects at the blastocyst stage. *In vitro* fertilization was performed with *Srsf7* heterozygous mutant sperm and ova to analyze development into morulae and blastocysts. *Srsf7*-homozygous KO embryos ($Srsf7^{fs/fs}$) successfully developed into blastocysts, clarifying that the embryonic lethality of *Srsf7*-KO mice occurred after the blastocyst stage and during the implantation stage (Figures S4D–S4F). Taken together, these results show that *Srsf7* is indispensable for the implantation stage of mouse development.

The embryonic lethality hampered the analysis of homozygous KO mice. Heterozygous *Srsf7*-KO mice were viable and fertile, but they exhibited impaired body growth. Both male and female $Srsf7^{WT/fs}$ mice exhibited lower body weight than the WT controls (Figures 4A and 4B), indicating that *Srsf7* is necessary for body growth in mice. The significant difference of body weight was observed also in the neonatal phase (Figure S5A). To gain an insight into a role for *Srsf7* in the protein synthesis *in vivo*, we investigated the expression of proteins associated with the activity of the protein synthesis. The expression of phosphorylated S6 and phosphorylated 4E-BP1 was suppressed in the *Srsf7* mutant tissues (Figures S5B and S5C). These findings implied that *Srsf7* might play a role in the regulation of protein synthesis also *in vivo*. To assess the machinery underlying the growth impairment of *Srsf7* mutant mice, we compared the gene expression profiles of WT and *Srsf7* mutants via RNA-seq (Figure 4C).

Heatmap analysis revealed that a subset of genes (1,716 genes) was suppressed by the *Srsf7* mutation throughout the CC, CMs, and Heps (Figure 4D). The subset included numerous JAGs and translation-associated genes (Figure 4D). The GO analysis revealed that this gene subset was associated with "translation" ($p < 10^{-33}$) and "ribosome" ($p < 10^{-39}$) (Figure 4E). These findings suggested that translation was dysregulated in the *Srsf7* mutant mice. Additionally, the *Srsf7* mutation showed a significantly more profound effect on the JAGs than on constitutively expressed genes, demonstrating that Srsf7 is indispensable for the expression of JAGs (Figure 4F). Among the JAGs, the expression of *Igf2* was suppressed significantly in CMs and Heps (Figure S5D). *Igf2* encodes a peptide that functions as a potent enhancer of body growth (DeChiara et al., 1990; Sun et al., 1997). The Igf2 suppression was observed also at the protein level in *Srsf7* mutant hearts and livers (Figure S5E). We also addressed physiological consequences of the aberrant ADAS in the *Srsf7* mutant mice. The GO analysis in the *Srsf7* mutant CC revealed that genes associated with myelination were affected significantly (Figures S6A), revealing the downregulation of myelin sheath-associated genes (Figure S6B). Immunostaining of myelin basic protein (MBP) revealed poorer myelination in the *Srsf7* mutant compared with WT (Figures S6C and S6D), whereas the neuronal formation was unaffected (Figures S6E and S6F). Thus, the *Srsf7* mutant mice showed the slight impairment of myelination in the CC. Together, the *Srsf7* mutation causes physiological deteriorations in the body growth and myelination that is accompanied by compromised expression of genes associated with translation and JAGs in mice.

Srsf7 Mediates ADAS

We next evaluated ADAS in the *Srsf7* mutant mice. MISO analysis revealed significantly (Bayes factor > $10^{1/2}$) and recurrently altered AS events in the *Srsf7* mutant mice (Figure 5A). The cutoff we used for determining true AS events almost completely excluded background or "noise" AS events, as shown by the fact that comparisons

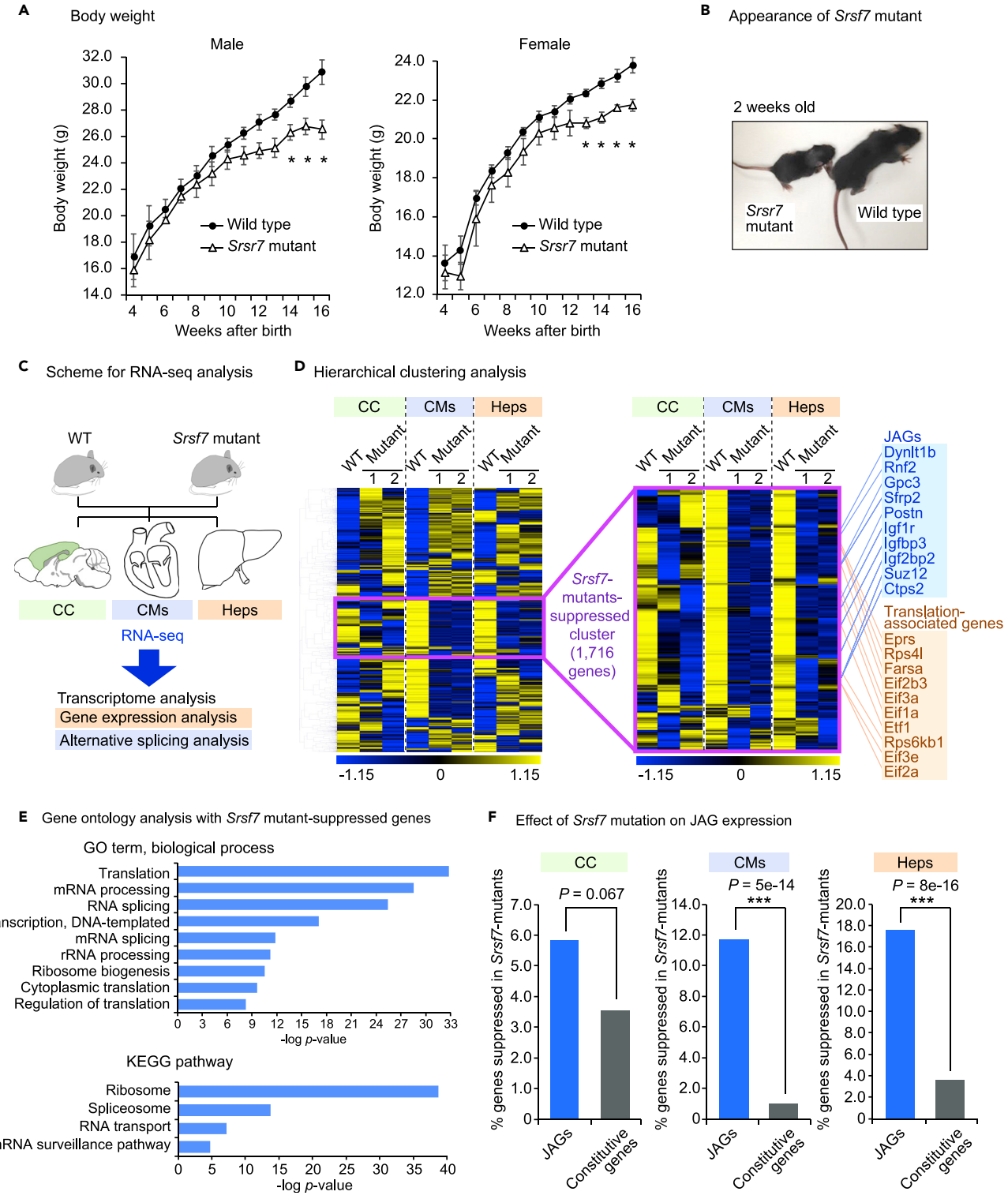

Figure 4. *Srsf7* Regulates Growth and JAGs in Mice

(A) The body weights of WT and *Srsf7*-heterozygous mutant mice (numbers of mice analyzed: WT male, 12; mutant male, 19; WT female, 17; mutant female, 14).

(B) Appearances of WT and *Srsf7* mutant mice at age 2 weeks.

(C) A schematic describing the RNA-seq analysis with CC, CMs, and Heps isolated from WT and *Srsf7* mutant mice. Two Srsf7 mutant mice and one WT littermate control were subjected to the RNA-seq analysis.

Figure 4. *Continued*

(D) Heatmap analysis of the RNA-seq results in CC, CMs, and Heps of WT and *Srsf7* mutant mice. The cluster of genes with a tendency to be downregulated in the three organs is magnified to the right. A partial list of JAGs and translation-associated genes included in the cluster is shown.

(E) Gene Ontology (GO) analysis of the *Srsf7* mutant-suppressed cluster. The biological processes and Kyoto Encyclopedia of Genes and Genomes (KEGG) pathways significantly associated with the cluster are shown.

(F) Frequencies of juvenility-associated genes (JAGs) and constitutively expressed genes among the $Srsf7^{WT/fs}$-suppressed genes. The *Srsf7* mutation affects JAGs more strongly than constitutively expressed genes.

* $p < 0.05$ and *** $p < 0.001$, Student's t test. Data are represented as the means ± standard deviations. See also Figures S4–S6.

among WT mice showed few AS events ("Background AS events" in Figure 5A). We performed GO analysis to predict the biological functions associated with the mis-spliced genes, and the results showed that, in addition to the expected "alternative splicing" (10^{-153}) (Figure 5B), functions such as "phosphoprotein" (10^{-110}) and "acetylation" (10^{-46}) were highly significantly enriched. These findings indicate that *Srsf7* exerts its influence through these enriched functions. We next asked whether Srsf7 mediated the ADAS that was observed earlier in this study. We investigated an overlap between the ADAS-target genes and the genes undergoing Srsf7-dependent AS. Overlaps of 33.1%, 41.8%, and 43.5% were observed between the ADAS-target genes and Srsf7-spliced genes in the CC, CMs, and Heps with statistical significance of 2×10^{-102}, 3×10^{-91}, and 8×10^{-71}, respectively (Figure 5C). These observations indicate that Srsf7 mediates a considerable portion of ADAS, thus establishing a role for Srsf7 in the age-dependent transition of the transcriptome.

Srsf7 Mediates ADAS in *Eif4a2* and *Rbm7*

We next sought to describe Srsf7-mediated ADAS in a gene-specific manner. We focused on the *Eif4a2* and *Rbm7* mRNAs, which underwent Srsf7-dependent AS at high significance (Bayes factor > $10^{1/2}$). *Eif4a2* underwent ADAS in which exon 11 (E11) was included in the juvenile form and excluded from the adult form throughout the CC, CMs, and Heps (Figure 6A). Because of a premature stop codon in E11, the juvenile form was shortened and lacked one-third of the C-terminal RNA helicase domain (Figure 6B), losing two beta-strands and two alpha-helixes of the RNA helicase domain compared with the adult form (Figure S5). However, E11 was skipped in *Srsf7* mutant organs even in juveniles, leading to the expression of the adult form of *Eif4a2* (Figure 6C). This finding was corroborated by qPCR, which distinguishably measured the two isoforms (Figure 6D).

Rbm7, a gene encoding an RBP associated with snoRNA biogenesis, underwent ADAS in which E2 was included in the juvenile form and excluded from the adult form throughout the CC, CMs, and Heps (Figure 6E). Because of a stop codon in E2, the juvenile form of *Rbm7* has an open reading frame of 39 amino acids (aa) in length, which is considerably shorter than the adult form, which consists of 265 aa (Figure 6F). Exon 2 was skipped in *Srsf7* mutant organs even in juveniles, thus yielding the adult form (Figure 6G). This finding was corroborated by qPCR (Figure 6H). Thus, our analysis revealed that Srsf7 mediates the ADAS of *Eif4a2* and *Rbm7*, causing switching from juvenile to adult isoforms.

Srsf7 Is Responsible for ADAS and Establishes the Juvenile Transcriptome

To assess the regulation of AS by Srsf7 more directly, we established an *in vitro* experimental platform for the analysis of Srsf7-mediated AS. We cloned the genomic sequences of *Eif4a2* and *Rbm7* and constructed minigene plasmids. The AS of *Eif4a2* and *Rbm7* were assessed in the *Srsf7*-KO Neuro2a cell lines (Figure 7A). The minigene assays revealed that *Srsf7*-KO causes the switching of isoforms from juvenile to adult for both *Eif4a2* (Figure 7B) and *Rbm7* (Figure 7C). Furthermore, RNA immunoprecipitation (RIP)-qPCR analysis revealed the binding of *Srsf7* protein to the *Eif4a2* RNA and *Rbm7* RNA (Figure 7D). These findings indicate that the Srsf7 protein directly mediates the AS of *Eif4a2* and *Rbm7*.

Thus, Srsf7 mediates the ADAS of the numerous transcripts including *Eif4a2* and *Rbm7*. The influences of *Srsf7* mutation was observed for the splicing of the significant number of genes that were also regulated by ADAS. ADAS enables higher anabolic potentials in juvenile animals through enhancing JAGs and translation-associated genes.

DISCUSSION

The age dependency of AS has not been well elucidated, and implications of ADAS for physiology and pathogenesis remain obscure. Here, we present a comprehensive view of ADAS during postnatal growth in a mouse model. Srsf7 mediates the ADAS of numerous genes including *Eif4a2* and *Rbm7*. Srsf7

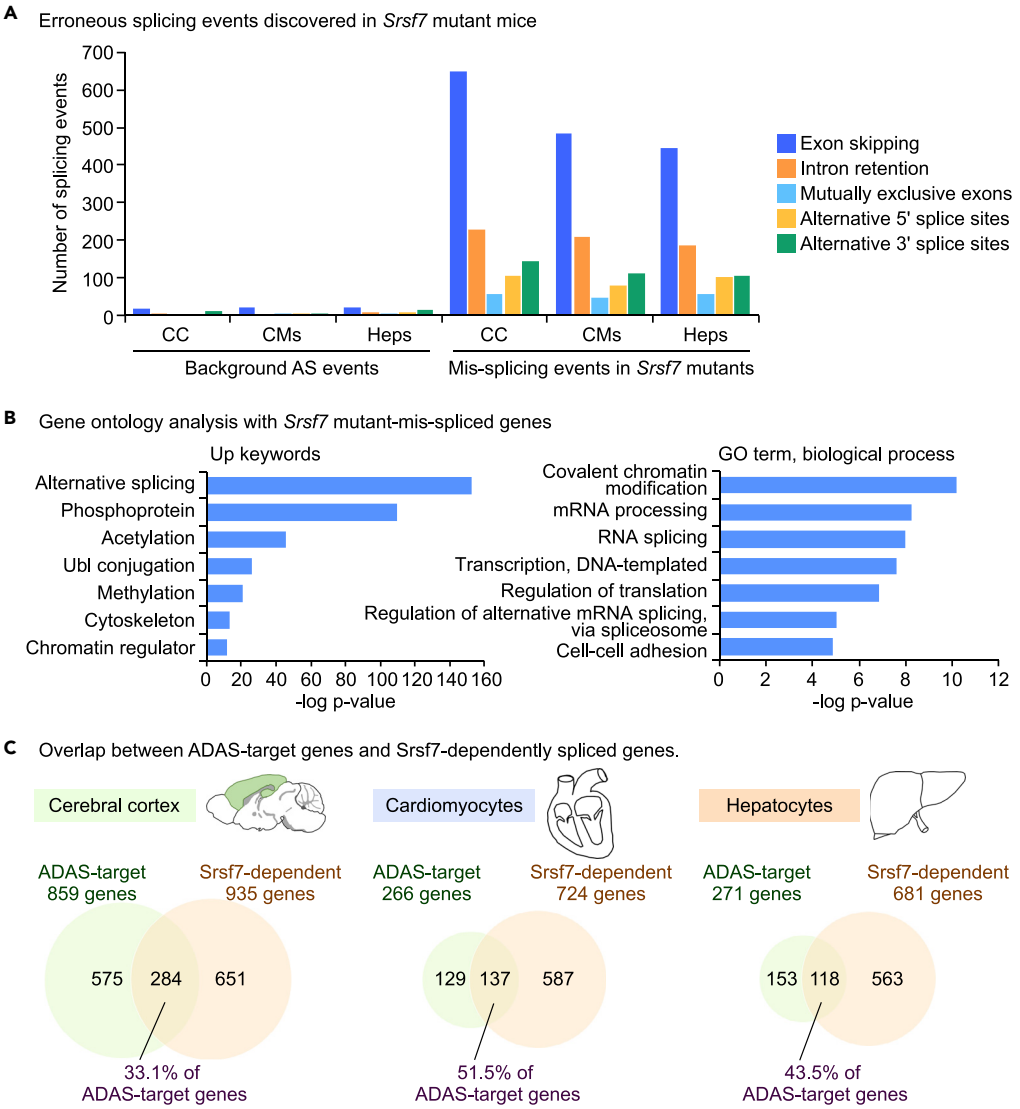

Figure 5. *Srsf7* Mediates ADAS in Mice

(A) Number of AS events detected in *Srsf7* mutant mice in comparison with WT mice (right half, "Mis-splicing events in *Srsf7* mutants"). Comparisons were also made between WT mice to show the background noise levels (left half, "Background AS events").

(B) Gene Ontology (GO) analysis of the genes that were mis-spliced in *Srsf7* mutant mice. "Up keywords" and "Biological processes" significantly associated with the mis-spliced genes are indicated.

(C) Venn diagrams to show overlaps between the ADAS-target genes and the genes mis-spliced in the *Srsf7* mutant.

contributes to the establishment of the juvenile transcriptome, which is characterized by the expression of JAGs and translation-associated genes, thus underlying the anabolic status of juvenile animals (Figure 7E).

Although AS has been investigated in terms of tissue- or cell-type specificity, its age dependency has not been comprehensively studied. The juvenile phase is characterized by distinct physiological features, such as growth and maturation, and by distinct gene expression profiles enriched in JAGs (Jam et al., 2018). This ADAS analysis revealed a previously undefined landscape of AS events, unmasking the regulatory layer of gene expression underlying the postnatal growth phase. Our findings indicate that the postnatal growth phase is underlain by splicing-based modifications of the transcriptome, which account for the anabolic status of juvenile animals and the expression of JAGs and translation-associated genes, thus contributing to juvenile properties.

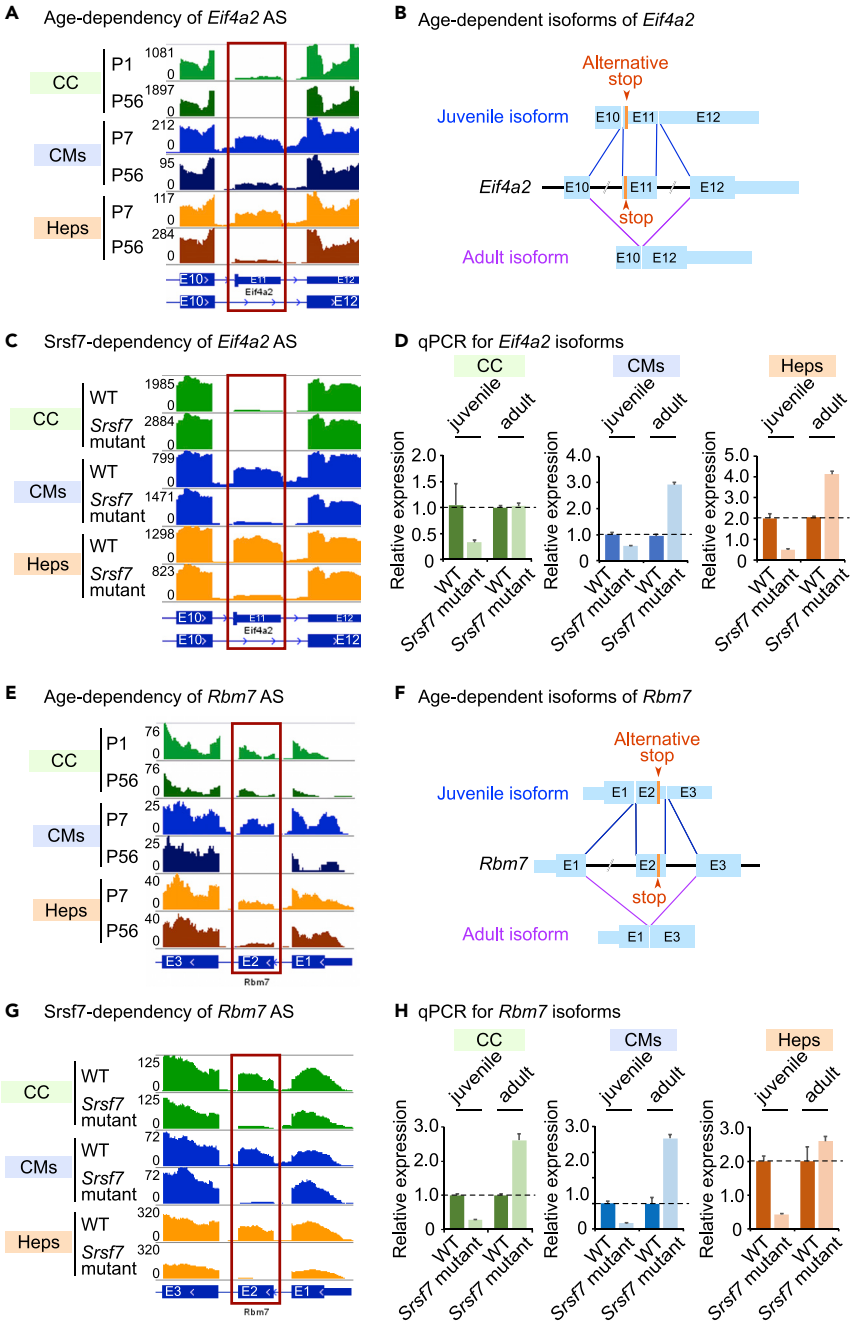

Figure 6. *Srsf7* Mediates ADAS of *Eif4a2* and *Rbm7*

(A) *Eif4a2* mRNA expression pattern in the juvenile and adult phases. Exon 11 (E11) is predominantly included in the juvenile phase compared with the adult phase.

(B) Schematic of the splicing isoforms of *Eif4a2*. E11 is included in the juvenile isoform and not in the adult isoform. E11 contains the alternative stop codon, thus generating a shorter protein.

(C) *Eif4a2* mRNA expression patterns in WT and *Srsf7* mutant organs. E11 is included in WT but not in *Srsf7* mutants. The *Srsf7* mutants thus express the adult form despite the mice being juvenile.

(D) qPCR analysis of the *Eif4a2* juvenile and adult isoforms in WT and *Srsf7* mutant mouse tissues (n = 3). Data were normalized to *Tubb5*.

(E) *Rbm7* mRNA expression patterns in the juvenile and adult phases. E2 is more frequently included in juveniles than in adults.

Figure 6. *Continued*

(F) Schematic of the splicing isoforms of *Rbm7*. E2 is included in the juvenile isoform and not in the adult isoform. E2 contains the alternative stop codon that terminates translation.

(G) *Rbm7* mRNA expression pattern in WT and *Srsf7* mutant organs. E2 is included in WT but not in *Srsf7* mutants. The *Srsf7* mutants thus express the adult form despite the mice being juvenile.

(H) qPCR analysis of *Rbm7* juvenile and adult isoforms in WT and *Srsf7* mutant mouse tissues (n = 3). Data were normalized to *Tubb5*.

Data are represented as the means ± standard deviations. See also Figure S7.

Cellular juvenescence is characterized by the cellular capacities for growth, maturation, differentiation, anabolic metabolism, and resistance to premature senescence (Tano et al., 2019). Cellular juvenescence is lost under suppression of the JALNC Gm14230 (Tano et al., 2019). Here, we showed that Srsf7 depletion also led to a loss of cellular juvenescence, in that cells exhibited impaired growth, differentiation, anabolism, and resistance to premature senescence. As evidenced by experiments in cells and mice, Srsf7 depletion led to decreased phosphorylation of S6, indicating suppressed protein synthesis. Thus, Srsf7 regulates anabolism through protein synthesis both *in vitro* and *in vivo*.

The Srsf7 protein showed nuclear localization, consistent with a splicing function. The nuclear expression of Srsf7 was lost at higher density, zeocin treatment, and RasV12-induced senescence. Srsf7 was not observed to translocate out of the nucleus, suggesting that the Srsf7 protein is regulated by its expression level and not by subcellular localization in the contexts we examined. The cell-density-dependent expression of the Srsf7 protein implied that Srsf7 may control anabolism in response to cell density. Srsf7 expression was also dependent on cellular juvenescence and was lost in RasV12-induced cellular senescence. The genotoxicity of zeocin may induce cell-cycle arrest, and it may also induce loss of cellular juvenescence through the suppression of Srsf7.

The homozygous null mutation of *Srsf7* caused early embryonic lethality, indicating its essentiality in the implantation stage. Homozygous mutations of *Srsf3*, the gene with the greatest similarity to *Srsf7*, cause defects in blastocyst formation before the implantation stage (Jumaa et al., 1999). This discrepancy demonstrates the non-redundant roles of *Srsf3* and *Srsf7* in blastocyst formation and the implantation stage, respectively.

Although our previous study found that the postnatal growth phase was characterized by age-dependent alteration of the transcriptome, the functional relevance of AS has not been elucidated (Jam et al., 2018). Not only did the juvenile transcriptome undergo extensive genome-wide AS, but we also identified *Srsf7* as a crucial factor for its regulation. *Srsf7* mutation caused erroneous ADAS that resulted in premature loss of JAGs and translation-associated genes. The ADAS events were "fast-forwarded," and premature switching from juvenile to adult isoforms took place. This effect was recapitulated by *in vitro* experiments in Neuro2a cells with null mutations of *Srsf7*, where the juvenile Eif4a2 and Rbm7 isoforms were switched to the adult isoforms prematurely.

We demonstrated that *Eif4a2* and *Rbm7* are direct targets of Srsf7. Srsf7 mediates the inclusion of E11 that contains the alternative stop codon; thus, the juvenile isoform lacks the part of the RNA helicase domain that is crucial for microRNA-mediated translational suppression. Eif4a2 is an ATP-dependent RNA helicase (Jackson et al., 2010) that is essential for microRNA-mediated translational repression (Meijer et al., 2013). Thus, the shortening of the RNA helicase domain is considered to cause dysregulation of microRNA-mediated translational repression, leading to increased protein expression. microRNA-mediated regulation of growth is also regulated at the level of microRNA biogenesis, which is enhanced by Hippo signaling (Mori et al., 2014). Srsf7-mediated AS of *Eif4a2* may function as a new regulatory layer of microRNA-mediated growth control. Rbm7, together with ZCCHC8 and hMTR4, constitutes the nuclear exosome targeting (NEXT) complex that directs a subset of RNAs, including snoRNA, toward exosomal degradation (Fan et al., 2017; Kufel and Grzechnik, 2019; Lubas et al., 2015; Ogami et al., 2018). Srsf7 mediates the splicing of the juvenile isoform that includes E2 and a premature stop codon, thus expressing a considerably shorter isoform lacking a part of the RNA recognition motif. The juvenile *Rbm7* isoform spares snoRNAs from degradation, promoting the translation process.

Our findings clarified previously unreported roles for ADAS in the establishment of the juvenile transcriptome and the anabolic status of juvenile animals. Our analysis suggested a more quantitative analysis for

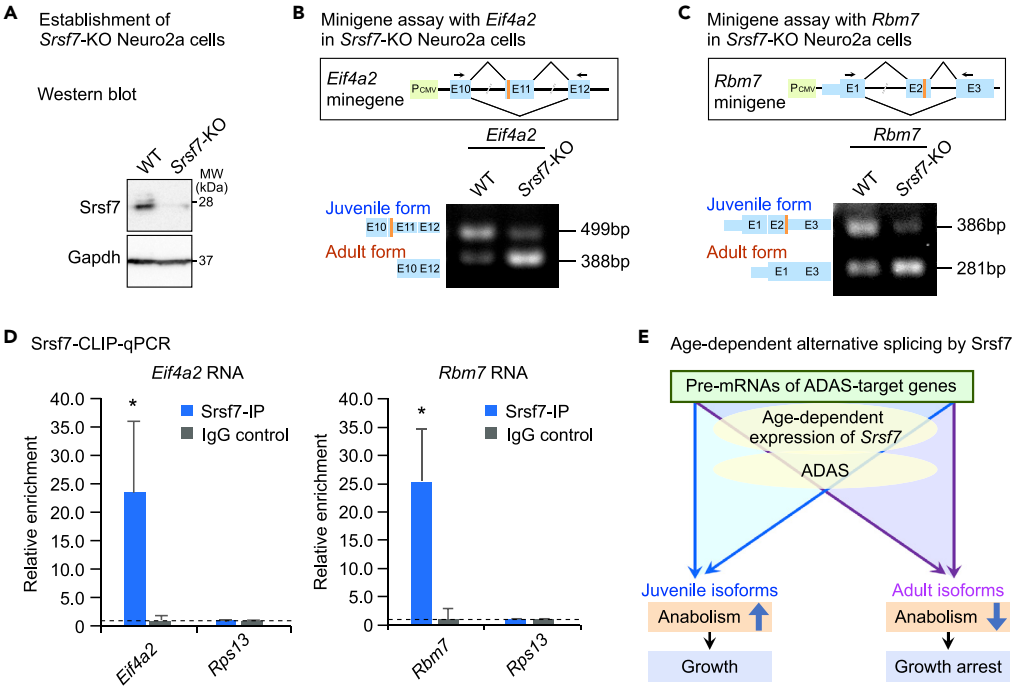

Figure 7. Srsf7 Mediates Isoform Switching of *Eif4a2* and *Rbm7*

(A) Western blot analysis for Srsf7 in WT and *Srsf7*-KO Neuro2a cell lines. Gapdh was analyzed for the loading control.

(B) Minigene assay with the *Eif4a2* gene construct. The scheme above shows the plasmid constructed to express exons 10–12 (E10–E12) of mouse *Eif4a2*. The primers used to detect the splicing products are indicated with arrows, and the RT-PCR results are shown below. *Srsf7*-KO induces switching of isoforms from juvenile to adult.

(C) Minigene assay with the *Rbm7* gene construct. The scheme above shows the plasmid constructed to express E1–E3 of mouse *Rbm7*. The primers used to detect the splicing products are indicated with arrows, and the RT-PCR results are shown below. *Srsf7*-KO induces switching of isoforms from juvenile to adult.

(D) RIP-qPCR was performed in Neuro2a cells after UV-cross-linking followed by immunoprecipitation with the Srsf7 antibody. qPCR was performed for *Eif4a2*, *Rbm7*, and the control, *Rps13*. Fold enrichment was calculated by normalizing to IgG.

(E) Schematic describing the role of Srsf7 in ADAS, thus establishing the juvenile transcriptome underlying the anabolic state in juveniles.

* $p < 0.05$, Student's t test. Data are represented as the means ± standard deviations.

AS. Our work implied a possibility that a particular SF may account for the splicing of a portion of a gene transcript and plural SFs contribute to the completion of the splicing of the particular gene. Future works that analyze the contributions of multiple SFs to the particular splicing pattern will clarify how SFs cooperate in the regulation of splicing. Also, in this study, we investigated the AS at the RNA level and not at the proteomic level. Further analysis at the proteomic level will reveal a functional consequence of the RNA splicing on the protein functions. Because AS has numerous implications in pathogenesis, further elucidation of the AS program and the roles of Srsf7 should lead to new therapeutics for intractable diseases, especially of children, in contexts where the juvenile properties and juvenile transcriptome are considered to be compromised. Through the AS, Srsf7 mediates the anabolic functions of the cells. By utilizing the function of Srsf7 to promote anabolism, it might be possible to enhance the growth or regenerative capacity of the organs, for the purpose of treating the intractable diseases without effective treatments or treatment via organ transplantation.

Here, we reported a comprehensive list of ADAS events in the postnatal organs and showed that the splicing of the significant number of ADAS-target genes is mediated by Srsf7. Srsf7 mediates juvenile patterns of AS, thus giving rise to the juvenile transcriptome. Mutation of *Srsf7* causes a premature switch from the juvenile to adult isoforms of at least *Eif4a2* and *Rbm7* both *in vitro* and *in vivo*, resulting in suppressed anabolism and impaired growth. Thus, the Srsf7-mediated ADAS establishes the juvenile transcriptome that underlies juvenile properties.

Limitations of the Study

- Our AS analysis was performed with a bulk of cells, not single cells. Our analysis implied that different types of AS might occur in a single cell. Future work at the single-cell resolution will reveal how different types of AS occur in transcripts from the same gene.
- Our analysis has not determined the comparable contribution of Srsf7 to AS among different SFs. Plural SFs may target to the same gene locus. Future work may make it possible to quantitatively compare the contributions of different SFs.

METHODS

All methods can be found in the accompanying Transparent Methods supplemental file.

DATA AND CODE AVAILABILITY

The accession numbers for the high throughput sequencing data reported in this paper are DNA Data Bank of Japan (DDBJ): DRA009510, DRA009537 and DRA009538.

SUPPLEMENTAL INFORMATION

Supplemental Information can be found online at https://doi.org/10.1016/j.isci.2020.100929.

ACKNOWLEDGMENTS

We would like to thank all the laboratory members of the Molecular Neuroscience Research Center (MNRC) for the helpful discussion and sincere cooperation. We would like to especially thank Jean-Pierre Bellier for repeated critical readings. This research was cooperated by the Central Research Laboratory at Shiga University of Medical Science (SUMS). M.M. is supported by a research grant from the Sumitomo Foundation, the Kato Memorial Bioscience Foundation, the Japan Epilepsy Research Foundation (JERF), the Houston Foundation, the MSD Life Science Foundation, the Ichiro Kanehara Foundation for the Promotion of Medical Sciences and Medical Care, and the Japan Brain Foundation. This study was supported by MEXT KAKENHI Grant Number 15K15387; JSPS KAKENHI Grant Numbers 15K15387, 15H01486, 18K07788, 19H04774; the Leading Initiative for Excellent Young Researchers (LEADER) 5013323; and Japan Agency for Medical Research and Development (AMED).

AUTHOR CONTRIBUTIONS

Y.K., F.A.J., H.Y., and M.M. conducted most of the experiments and analyzed the data. Y.K. and M.M. performed bioinformatics analysis. F.A.J. and M.M. performed mouse experiments. H.Y. and M.M. conducted cellular experiments. I. Terakado performed *in vitro* development experiments. T.M. conducted gene expression analysis and assisted cell culture experiments. A.T., Y.T., S.A., and M.F. assisted experiment and data analysis. I. Tooyama assisted in the data analysis and discussed the results with M.M. M.M conceived the experiment and wrote the manuscript. All authors reviewed the manuscript.

DECLARATION OF INTERESTS

The authors declare no competing interests.

Received: October 17, 2019
Revised: January 26, 2020
Accepted: February 17, 2020
Published: March 27, 2020

REFERENCES

Alt, F.W., Bothwell, A.L.M., Knapp, M., Siden, E., Mather, E., Koshland, M., and Baltimore, D. (1980). Synthesis of secreted and membrane-bound immunoglobulin mu heavy chains is directed by mRNAs that differ at their 3′ ends. Cell *20*, 293–301.

Anders, G., Mackowiak, S.D., Jens, M., Maaskola, J., Kuntzagk, A., Rajewsky, N., Landthaler, M., and Dieterich, C. (2012). doRiNA: a database of RNA interactions in post-transcriptional regulation. Nucleic Acids Res. *40*, 180–186.

Baker, B.S. (1989). Sex in flies: the splice of life. Nature *340*, 521–524.

Barbosa-Morais, N.L., Irimia, M., Pan, Q., Xiong, H.Y., Gueroussov, S., Lee, L.J., Slobodeniuc, V., Kutter, C., Watt, S., Colak, R., et al. (2012). The evolutionary landscape of alternative splicing in vertebrate species. Science *338*, 1587–1593.

Berget, S.M., Moore, C., and Sharp, P.A. (1977). Spliced segments at the 5′ terminus of adenovirus 2 late mRNA. Proc. Natl. Acad. Sci. U S A *74*, 3171–3175.

Blanco, F.J., and Bernabéu, C. (2012). The splicing factor SRSF1 as a marker for endothelial senescence. Front. Physiol. *3*, 1–6.

Blekhman, R., Marioni, J.C., Zumbo, P., Stephens, M., and Gilad, Y. (2010). Sex-specific and lineage-specific alternative splicing in primates. Genome Res. *20*, 180–189.

Cavaloc, Y., Bourgeois, C.F., Kister, L., and Stévenin, J. (1999). The splicing factors 9G8 and SRp20 transactivate splicing through different and specific enhancers. RNA *5*, 468–483.

Chen, M., and Manley, J.L. (2009). Mechanisms of alternative splicing regulation: insights from molecular and genomics approaches. Nat. Rev. Mol. Cell Biol. *10*, 741–754.

Chen, Z., Trotman, L.C., Shaffer, D., Lin, H.-K., Dotan, Z.A., Niki, M., Koutcher, J.A., Scher, H.I., Ludwig, T., Gerald, W., et al. (2005). Crucial role of p53-dependent cellular senescence in suppression of Pten-deficient tumorigenesis. Nature *436*, 725–730.

Chow, L.T., Gelinas, R.E., Broker, T.R., and Roberts, R.J. (1977). An amazing sequence arrangement at the 5′ ends of adenovirus 2 messenger RNA. Cell *12*, 1–8.

Cieply, B., and Carstens, R.P. (2015). Functional roles of alternative splicing factors in human disease. Wiley Interdiscip. Rev. RNA *6*, 311–326.

Cong, L., Ran, F.A., Cox, D., Lin, S., Barretto, R., Habib, N., Hsu, P.D., Wu, X., Jiang, W., Marraffini, L.A., and Zhang, F. (2013). Multiplex genome engineering using CRISPR/Cas systems. Science *339*, 819–823.

DeChiara, T.M., Efstratiadis, A., and Robertsen, E.J. (1990). A growth-deficiency phenotype in heterozygous mice carrying an insulin-like growth factor II gene disrupted by targeting. Nature *345*, 78–80.

Denchi, E.L., Attwooll, C., Pasini, D., and Helin, K. (2005). Deregulated E2F activity induces hyperplasia and senescence-like features in the mouse pituitary gland. Mol. Cell. Biol. *25*, 2660–2672.

Early, P., Rogers, J., Davis, M., Calame, K., Bond, M., Wall, R., and Hood, L. (1980). Two mRNAs can be produced from a single immunoglobulin μ gene by alternative RNA processing pathways. Cell *20*, 313–319.

Ellis, J.D., Barrios-Rodiles, M., Çolak, R., Irimia, M., Kim, T.H., Calarco, J.A., Wang, X., Pan, Q., O'Hanlon, D., Kim, P.M., et al. (2012). Tissue-specific alternative splicing remodels protein-protein interaction networks. Mol. Cell *46*, 884–892.

Erkelenz, S., Mueller, W.F., Evans, M.S., Busch, A., Schöneweis, K., Hertel, K.J., and Schaal, H. (2013). Position-dependent splicing activation and repression by SR and hnRNP proteins rely on common mechanisms. RNA *19*, 96–102.

Escudero-Paunetto, L., Li, L., Hernandez, F.P., and Sandri-Goldin, R.M. (2010). SR proteins SRp20 and 9G8 contribute to efficient export of herpes simplex virus 1 mRNAs. Virology *401*, 155–164.

Fan, J., Kuai, B., Wu, G., Wu, X., Chi, B., Wang, L., Wang, K., Shi, Z., Zhang, H., Chen, S., et al. (2017). Exosome cofactor hMTR4 competes with export adaptor ALYREF to ensure balanced nuclear RNA pools for degradation and export. EMBO J. *36*, 2870–2886.

Giulietti, M., Piva, F., D'Antonio, M., De Meo, P.D.O., Paoletti, D., Castrignanò, T., D'Erchia, A.M., Picardi, E., Zambelli, F., Principato, G., et al. (2013). SpliceAid-F: a database of human splicing factors and their RNA-binding sites. Nucleic Acids Res. *41*, 125–131.

Han, H., Irimia, M., Ross, P.J., Sung, H.-K., Alipanahi, B., David, L., Golipour, A., Gabut, M., Michael, I.P., Nachman, E.N., et al. (2013). MBNL proteins repress ES-cell-specific alternative splicing and reprogramming. Nature *498*, 241–245.

Hensch, T.K. (2005). Critical period plasticity in local cortical circuits. Nat. Rev. Neurosci. *6*, 877–888.

Inui, M., Miyado, M., Igarashi, M., Tamano, M., Kubo, A., Yamashita, S., Asahara, H., Fukami, M., and Takada, S. (2015). Rapid generation of mouse models with defined point mutations by the CRISPR/Cas9 system. Sci. Rep. *4*, 5396.

Jackson, R.J., Hellen, C.U.T., and Pestova, T.V. (2010). The mechanism of eukaryotic translation initiation and principles of its regulation. Nat. Rev. Mol. Cell Biol. *11*, 113–127.

Jam, F.A., Kadota, Y., Mendsaikhan, A., Tooyama, I., and Mori, M. (2018). Identification of juvenility-associated genes in the mouse hepatocytes and cardiomyocytes. Sci. Rep. *8*, 3132.

Jeong, S. (2017). SR proteins: binders, regulators, and connectors of RNA. Mol. Cells *40*, 1–9.

Jumaa, H., Wei, G., and Nielsen, P.J. (1999). Blastocyst formation is blocked in mouse embryos lacking the splicing factor SRp20. Curr. Biol. *9*, 899–902.

Katz, Y., Wang, E.T., Airoldi, E.M., and Burge, C.B. (2010). Analysis and design of RNA sequencing experiments for identifying isoform regulation. Nat. Methods *7*, 1009–1015.

Kim, J.W., Tchernyshyov, I., Semenza, G.L., and Dang, C.V. (2006). HIF-1-mediated expression of pyruvate dehydrogenase kinase: a metabolic switch required for cellular adaptation to hypoxia. Cell Metab. *3*, 177–185.

Kluza, J., Corazao-Rozas, P., Touil, Y., Jendoubi, M., Maire, C., Guerreschi, P., Jonneaux, A., Ballot, C., Balayssac, S., Valable, S., et al. (2012). Inactivation of the HIF-1α/PDK3 signaling axis drives melanoma toward mitochondrial oxidative metabolism and potentiates the therapeutic activity of pro-oxidants. Cancer Res. *72*, 5035–5047.

Kohtz, J.D., Jamison, S.F., Will, C.L., Zuo, P., Lührmann, R., Garcia-Blanco, M.A., and Manley, J.L. (1994). Protein–protein interactions and 5′-splice-site recognition in mammalian mRNA precursors. Nature *368*, 119–124.

Kon, S., Ishibashi, K., Katoh, H., Kitamoto, S., Shirai, T., Tanaka, S., Kajita, M., Ishikawa, S., Yamauchi, H., Yako, Y., et al. (2017). Cell competition with normal epithelial cells promotes apical extrusion of transformed cells through metabolic changes. Nat. Cell Biol. *19*, 530–541.

Kufel, J., and Grzechnik, P. (2019). Small nucleolar RNAs tell a different tale. Trends Genet. *35*, 104–117.

Long, J.C., and Caceres, J.F. (2009). The SR protein family of splicing factors: master regulators of gene expression. Biochem. J. *417*, 15–27.

Lubas, M., Andersen, P.R., Schein, A., Dziembowski, A., Kudla, G., and Jensen, T.H. (2015). The human nuclear exosome targeting complex is loaded onto newly synthesized RNA to direct early ribonucleolysis. Cell Rep. *10*, 178–192.

Mali, P., Yang, L., Esvelt, K.M., Aach, J., Guell, M., DiCarlo, J.E., Norville, J.E., and Church, G.M. (2013). RNA-guided human genome engineering via Cas9. Science *339*, 823–826.

Meijer, H.A., Kong, Y.W., Lu, W.T., Wilczynska, A., Spriggs, R.V., Robinson, S.W., Godfrey, J.D., Willis, A.E., and Bushell, M. (2013). Translational repression and eIF4A2 activity are critical for microRNA-mediated gene regulation. Science *340*, 82–85.

Mori, M., Triboulet, R., Mohseni, M., Schlegelmilch, K., Shrestha, K., Camargo, F.D., and Gregory, R.I. (2014). Hippo signaling regulates microprocessor and links cell-density-dependent miRNA biogenesis to cancer. Cell *156*, 893–906.

Nilsen, T.W., and Graveley, B.R. (2010). Expansion of the eukaryotic proteome by alternative splicing. Nature *463*, 457–463.

Ogami, K., Chen, Y., and Manley, J. (2018). RNA surveillance by the nuclear RNA exosome: mechanisms and significance. Non Coding RNA *4*, https://doi.org/10.3390/ncrna4010008.

Pan, Q., Shai, O., Lee, L.J., Frey, B.J., and Blencowe, B.J. (2008). Deep surveying of alternative splicing complexity in the human transcriptome by high-throughput sequencing. Nat. Genet. *40*, 1413–1415.

Salomonis, N., Schlieve, C.R., Pereira, L., Wahlquist, C., Colas, A., Zambon, A.C., Vranizan, K., Spindler, M.J., Pico, A.R., Cline, M.S., et al. (2010). Alternative splicing regulates mouse embryonic stem cell pluripotency and differentiation. Proc. Natl. Acad. Sci. U S A *107*, 10514–10519.

Serrano, M., Lin, A.W., McCurrach, M.E., Beach, D., and Lowe, S.W. (1997). Oncogenic ras provokes premature cell senescence associated with accumulation of p53 and p16INK4a. Cell *88*, 593–602.

Shepard, P.J., and Hertel, K.J. (2009). The SR protein family. Genome Biol. *10*, 242.

Sun, F.L., Dean, W.L., Kelsey, G., Allen, N.D., and Reik, W. (1997). Transactivation of Igf2 in a mouse model of Beckwith-Wiedemann syndrome. Nature *389*, 809–815.

Tano, A., Kadota, Y., Morimune, T., Jam, F.A., Yukiue, H., Bellier, J.-P., Sokoda, T., Maruo, Y.,

Tooyama, I., and Mori, M. (2019). The juvenility-associated long noncoding RNA Gm14230 maintains cellular juvenescence. J. Cell Sci. *132*, https://doi.org/10.1242/jcs.227801.

Tazi, J., Bakkour, N., and Stamm, S. (2009). Alternative splicing and disease. Biochim. Biophys. Acta *1792*, 14–26.

Ule, J., Ule, A., Spencer, J., Williams, A., Hu, J.S., Cline, M., Wang, H., Clark, T., Fraser, C., Ruggiu, M., et al. (2005). Nova regulates brain-specific splicing to shape the synapse. Nat. Genet. *37*, 844–852.

Valente, S.T., Gilmartin, G.M., Venkatarama, K., Arriagada, G., and Goff, S.P. (2009). HIV-1 mRNA 3′ end processing is distinctively regulated by eIF3f, CDK11, and splice factor 9G8. Mol. Cell *36*, 279–289.

Venables, J.P., Klinck, R., Koh, C., Gervais-Bird, J., Bramard, A., Inkel, L., Durand, M., Couture, S., Froehlich, U., Lapointe, E., et al. (2009). Cancer-associated regulation of alternative splicing. Nat. Struct. Mol. Biol. *16*, 670–676.

Wajapeyee, N., Serra, R.W., Zhu, X., Mahalingam, M., and Green, M.R. (2008). Oncogenic BRAF induces senescence and apoptosis through pathways mediated by the secreted protein IGFBP7. Cell *132*, 363–374.

Wang, E.T., Sandberg, R., Luo, S., Khrebtukova, I., Zhang, L., Mayr, C., Kingsmore, S.F., Schroth, G.P., and Burge, C.B. (2008). Alternative isoform regulation in human tissue transcriptomes. Nature *456*, 470–476.

Warzecha, C.C., Sato, T.K., Nabet, B., Hogenesch, J.B., and Carstens, R.P. (2009). ESRP1 and ESRP2 are epithelial cell-type-specific regulators of FGFR2 splicing. Mol. Cell *33*, 591–601.

Wu, J.Y., and Maniatis, T. (1993). Specific interactions between proteins implicated in splice site selection and regulated alternative splicing. Cell *75*, 1061–1070.

Zhao, B.S., Roundtree, I.A., and He, C. (2016). Post-transcriptional gene regulation by mRNA modifications. Nat. Rev. Mol. Cell Biol. *18*, 31–42.

iScience, Volume *23*

Supplemental Information

Srsf7 Establishes the Juvenile Transcriptome through Age-Dependent Alternative Splicing in Mice

Yosuke Kadota, Faidruz Azura Jam, Haruka Yukiue, Ichiro Terakado, Takao Morimune, Ayami Tano, Yuya Tanaka, Sayumi Akahane, Mayu Fukumura, Ikuo Tooyama, and Masaki Mori

TRANSPARENT METHODS

Animal experiments

All animal experiments were approved by the institutional animal care and use committee of Shiga University of Medical Science. All experiments were performed in accordance with the relevant guidelines and regulations.

Establishment of *Srsf7* mutant mice

Reagents for genome editing

The *Srsf7* mutant mouse strains were generated using CRISPR-Cas9 technology as described previously (Inui et al., 2015). The C57BL/6N strain was used as the background strain. The guide RNA (gRNA) was designed using CRISPRdirect (https://crispr.dbcls.jp/). The target sequence of the gRNA is shown in **Table S1**. The gRNA sequence was cloned into the gRNA cloning vector (Addgene Plasmid ID #41824).

To assess gRNA quality, a T7 endonuclease assay was performed. The gRNA plasmid and hCas9 plasmid (Addgene plasmid ID #41815) were transfected into NIH3T3 cells using Lipofectamine 2000 transfection reagent (Thermo Fisher Scientific). Genome DNA was extracted using a Puregene DNA Extraction Kit (Qiagen). The genome sequence containing the target site was PCR-amplified with PrimeSTAR Max DNA polymerase (Takara Bio) with the primers shown in **Table S1**. After heat denaturation followed by reannealing, cleavage efficiency by T7 endonuclease I was assessed by agarose gel electrophoresis.

For gRNA synthesis, the T7 RNA polymerase recognition site was attached to the gRNA sequence via PCR. The PCR products were purified and used as the template for *in vitro* RNA synthesis using the mMESSAGE mMACHINE T7 Transcription Kit (Life Technologies). The synthesized gRNA was purified using MEGAclear (Ambion). Recombinant Cas9 protein was purchased (GeneArt Platinum Cas9 Nuclease, Thermo Fisher Scientific, B25642).

Microinjection

Mouse zygotes were obtained via *in vitro* fertilization (IVF) of WT C57BL/6N gametes. gRNA (100 ng/ml) and Cas9 protein (30 ng/ml, TrueCut Cas9 Protein v2, Invitrogen) were mixed and microinjected into the pro-nuclei and cytoplasm of zygotes, and the injected embryos were incubated at 37°C until they were transferred into pseudo-pregnant females at the two-cell stage.

Genotyping

Genomic DNA was extracted from the tail tips of pups, and the genomic sequence around the gRNA target site was PCR-amplified using the primers shown in **Table S1**. The obtained PCR products were treated with ExoSAP-IT (Thermo Fisher Scientific) and sequenced. Genotype was also determined by restriction enzyme cleavage at the AfI-II site, which was altered by the mutations described in this study. For the analyses of *Srsf7* mutant mice, both sexes of at least 4 different strains were analyzed. For the body weight analysis, body weight was measured with both sexes of mice on postnatal day 4 (P4), P7, P14 and once a week after 4 weeks old.

***In vitro* fertilization, generation and culture of preimplantation embryos**

Sperm or ova were taken from sexually mature *Srsf7* heterozygous mutant male or female mice, respectively. Female mice were superovulated by intraperitoneal administration of 0.15 ml (7.5 IU) / animal serum gonadotropin (Serotropin, ASKA Animal Health Co., Ltd) and 0.15 ml (7.5 IU) / animal placental gonadotropin (Gonatropin, ASKA Animal Health Co., Ltd) at the interval of 48 hours. HTF medium (ARK Resource) was used for IVF, and KSOM medium (ARK Resource) was used for embryo culture. Sperm were taken from the epididymis tail and resuspended in 100 µl of an HTF droplet in mineral oil (M5310, Sigma) on a 35 mm petri dish for 60 minutes at 37°C and 5% CO_2. The ova were taken from the ampulla of the uterine tube 16 hours after hormone administration and cultured in 200 µl of an HTP droplet in mineral oil

on a 35 mm petri dish at 37°C and 5% CO_2. Insemination was conducted by adding 4.5 μL precultured sperm resuspension into the ova-containing HTF droplet. Six hours after insemination, zygotes at the pronuclear stage were selected and transferred into 50 μl KSOM droplets within mineral oil and further cultured at 37°C and 5% CO_2. On the next day, zygotes that had proceeded to the 2-cell stage were selected and further cultured until Dpc5.5.

Genotyping of blastocysts with nested PCR

To genotype the blastocysts, nested PCR was performed. Blastocysts in 2 μl of buffer were lysed in PCR tubes by 3 cycles of heating at 98°C and freezing at -30°C. With 1 μl of the lysates as a template, the 1st round of PCR was performed using PrimeSTAR Max DNA Polymerase (Takara Bio) (30 cycles of 10 sec at 98°C, 5 sec at 55°C and 30 sec at 72°C). Nested PCR was performed using 0.2% of the 1st round PCR product as a template (20 cycles of 10 sec at 98°C, 5 sec at 55°C and 30 sec at 72°C). The primer sequences are shown in **Table S1**. Digestion with the Afl-II restriction enzyme was used to analyse the genotypes.

Cell culture

Neuro2a (male) or NIH3T3 (male) cell lines were cultured in Eagle's Minimum Essential Medium (EMEM) or Dulbecco's Modified Eagle's Medium (DMEM) containing 10% fetal bovine serum (FBS) and penicillin/streptomycin, respectively. To induce neural differentiation, retinoic acid was added to the culture medium at 20μM and incubated for 48 hours. For zeocin-induced cellular senescence model, cells were treated with zeocin at 80μg/ml for 96 hours. In the knockdown experiments, Lipofectamine RNAiMAX (Invitrogen) was used to transfect the siRNA duplexes at 10 nM: Mouse *Srsf7* siRNA1 (Bioneer, AccuTarget siRNA ID1424257), siRNA2 (ID1424259), and siRNA negative control (Applied Biosystems, AM4611). The knockdown efficiency was assessed 48 hours after transfection by qPCR or western blot analysis. The cell images were obtained using EVOS FL (Thermo Fisher Scientific). The number of cells per field was counted manually.

Inducible expression of *RasV12* in Neuro2a cells

Neuro2a cell strains that express *RasV12-EGFP* in the doxycycline-inducible manner were established by serial transfections of pcDNA6/TR and pcDNA4/TO-RasV12-EGFP. The plasmids were gifted by Shunsuke Kon and Yasuyuki Fujita (Hokkaido University, Japan). To induce *RasV12-EGFP*, the cell strains were treated with doxycycline at 2 μg/ml concentration for 96 hrs. For immunocytochemistry, cells were fixed with 4% PFA for 10 min at RT, followed by the membrane permeabilization with 0.1% Triton X-100 for 2 min at RT. The cells were then incubated with 2% FBS for blocking for 1 hr at RT. Then cells were incubated with the primary antibody against Srsf7 (1:200, Thermo Fisher Scientific, PA5-39482) and Vimentin (for the control condition, 1:80, Santa Cruz, sc-6260) for overnight at 4°C. After washing with PBS for 10 min 3 times, the cells were incubated with the secondary antibodies anti-rabbit-Alexa Fluor 546 and anti-mouse-Alexa Fluor 488 (1:1,000, Invitrogen) for 1 hr at RT. The cells were washed and mounted with Prolong Gold with DAPI (Thermo Fisher Scientific). Images were taken using a confocal microscope (Leica, TCS SP8).

To analyze the effect of *Srsf7* forced expression on *RasV12*-induced cellular senescence, pcDNA4-Srsf7 or control pcDNA4 empty plasmid was transfected to the Neuro2a-RasV12 cells, followed by the doxycycline treatment. To assess the cell shape enlargement, cells area were measured using Fiji (Schindelin et al., 2012). Those cells with area values >+2SD from the mean of the untreated control Neuro2a cells were counted as enlarged cells.

CRISPR-KO of *Srsf7* in Neuro2a cells

The gRNA plasmid used for the generation of *Srsf7*-KO mice and hCas9 plasmid were transfected into Neuro2a cells using Lipofectamine 2000 transfection reagent (Thermo Fisher Scientific). A limiting dilution method was used to clone the cell lines. A *Srsf7* genotype was determined by sequencing analysis. The clones that did not show any wild type sequence were selected and used for the analysis. The clones that did not show any mutation were used as WT control cell lines.

Gene expression analysis with qPCR

The total RNA was extracted using TRIzol reagent (Thermo Fisher Scientific). The extracted RNA was quantified using a NanoDrop Lite Spectrophotometer (Thermo Fisher Scientific) and reverse transcribed using a High-Capacity RNA-to-cDNA Kit (Applied Biosystems) and a PCR Thermal Cycler Dice (Takara) according to the manufacturer's instructions. qPCR was performed using a LightCycler 480 SYBR Green I Master Kit on a LightCycler 480 instrument (Roche) using the reverse transcribed cDNA as a template. The specificity and quality of the qPCR amplification was assessed by confirming a single band after agarose gel electrophoresis and a melting curve analysis. The data were normalized to control genes as indicated in the Figure legends. The primers used for the qPCR were listed in **Table S1**.

SDS-PAGE and western blot analysis

The cells were harvested in RIPA lysis buffer containing 25 mM Tris-HCl (pH 7.6), 150 mM NaCl, 1% NP-40, 1% sodium deoxycholate and 0.1% SDS. Mouse tissues were crushed using a homogenizer (μT-12, Taitec) in RIPA buffer, and the lysates were centrifuged at 20,400 ×g for at least 5 minutes to remove debris. Then, 5x Laemmli sample buffer was added to the lysates, followed by boiling at 95°C for 2 minutes (min). The protein samples (10 μg per lane) were separated by SDS-PAGE and transferred to a Hybond-P PVDF membrane (GE Healthcare). Western blotting was performed using the following antibodies: Srsf7 (1:1000, Thermo Fisher Scientific, PA5-39482), pS6 (1:1000, Cell Signaling Technology, #5364), S6 (1:1000, Cell Signaling Technology, #2217), p4E-BP1 (1:1000, Cell Signaling Technology, #2855), Pdk1 (1:1000, Cell Signaling Technology, #3820), Cox1 (mt-Co1, 1:1000, Abcam, ab14705), cMyc (1:1000, Cell Signaling Technology, #5605), YAP-S127P (1:1000, Cell Signaling Technology, #13008), LC3B (1:1000, Cell Signaling Technology, #2775S), p16 ARC (1:1000, Abcam, ab51243), p27 Kip1 (1:1000, Cell Signaling Technology, #3698), γH2ax (1:1000, Cell Signaling Technology, #9718), Igf2 (1:500, R&D Systems, MAB792-SP), Alpha/beta tubulin (1:1000, Cell Signaling Technology, #2148S), Gapdh (1:4000, Cell

Signaling Technology, #5174) and beta-actin (Actb) 13E5 HRP-conjugated (1:4000, Cell Signaling Technology, #5125). Secondary antibodies conjugated with horseradish peroxidase (Thermo Fisher Scientific, anti-mouse 32430 and anti-rabbit 32460) were used at 1:1000 dilution. The immunoreactive bands were detected using Chemi-Lumi One L or Chemi-Lumi One Ultra (Nacalai Tesque).

Immunocytochemistry

Neuro2a cells treated with zeocin or transfected with siRNA were fixed with 4% paraformaldehyde for 10 min at RT, permeabilized with 0.1% Triton X-100 for 2 min at RT, blocked with 2% FBS, and incubated with antibody against Srsf7 (1:200, Thermo Fisher Scientific, PA5-39482) and Vimentin (1:80, Santa Cruz, sc-6260) at 4°C overnight. After washing with PBS for 10 min 3 times, cells were incubated with anti-rabbit-Alexa Fluor 488 and anti-mouse-Alexa Fluor 546 (1:1,000, Invitrogen) for 1 hr at RT. After washing with PBS for 10 min 3 times, cells were mounted with Prolong Gold with DAPI (Invitrogen). Images were taken using a confocal microscope (Leica, TCS SP8).

Immunohistochemistry (IHC)

Brains were dissected from WT and *Srsf7* mutant mice at P7 and were fixed with 4% PFA for 3 hrs. The tissues were embedded in OCT compound and sectioned with a cryostat at 25 μm thickness. The floating sections were washed with PBS and blocked in PBS containing 2% FBS and 0.1% Triton X-100 for 1 hr at RT. The sections were incubated in primary antibody against MBP (1:400, Cell Signaling Technology, 78896) or Neurofilament L (1:1000, Cell Signaling Technology, #2837) overnight at 4°C. After washing with PBS for 15 min 3 times, sections were incubated in the secondary antibody anti-rabbit-Alexa Fluor 488 (1:1,000, Thermo Fisher Scientific) overnight at 4°C. After washing with PBS for 15 min 3 times, sections were mounted on glass slides with Prolong Gold with DAPI (Invitrogen). Images

were taken using a confocal microscope (Leica, TCS SP8). The pixel intensities were measured with FIJI (Schindelin et al., 2012).

Flux analysis

The oxygen consumption rate (OCR) and extracellular acidification rate (ECAR) were measured using an Agilent Seahorse XF Extracellular Flux Analyzer XFp (Seahorse Biosciences, MA). All tests were performed in accordance with the manufacturer's instructions and as described previously (Solis et al., 2016). Neuro2a cells transfected with control siRNA or *Srsf7* siRNA were seeded onto Seahorse XFp Cell Culture Miniplates (Seahorse Biosciences) at 12,000 cells per well and cultured for 48 hours. Before the metabolic analysis, cells were equilibrated in a non-CO_2 incubator with Seahorse calibration buffer for 60 minutes. Using the Seahorse XFp Cell Energy Phenotype Test Kit (Seahorse Biosciences), OCR and ECAR under baseline and stressed conditions were measured and normalized to the number of cells at the measurement.

Mitochondrial quantification

Relative mitochondrial quantity was estimated by measuring the amount of mitochondrial genome DNA relative to nuclear genome DNA. The genome DNA was extracted from Neuro2a cells 72 hrs after transfection of control siRNA or *Srsf7* siRNA (n=4) using DNeasy Blood and Tissue Kit (Qiagen). The quantitative real-time PCR was performed with primers against *16S* and *mt-Co1* for the mitochondrial and *18S* for the nuclear genome DNA. The ratio of mitochondrial/nuclear genome DNA were calculated. The ratios were further normalized to the control siRNA condition.

RNA immunoprecipitation (RIP)-qPCR

Crosslinking was performed by exposing the Neuro2a cells in culture dishes to UV (UV Crosslinker, FS-800, Funakoshi) (at 254 nm and at 4000 x 100 μjoules/cm^2 energy). The

culture medium was replaced with PBS before UV-crosslinking. The cells were lysed with lysis buffer containing 20 mM Tris-Cl, pH 8.0, 1 mM EDTA, 100 mM NaCl, and 0.5% (v/v) Nonidet P-40, 0.5% sodium deoxycholate, 0.05% SDS). The cell lysates were collected by scraping and treated with 10 units of Turbo DNase at 37°C for 10 minutes. After centrifugation at 20,000 ×g for 5 minutes at 4°C, a portion (10%) of the supernatant was collected as the input sample. Ten micrograms of *Srsf7* antibody (Thermo Fisher Scientific, #PA5-39482) and isotype control IgG (ab171870, Abcam) were conjugated to Dynabeads Protein A (10002D, Life Technologies) and incubated with the supernatants overnight at 4°C. The Dynabeads complexes were collected using a magnet stand (Dynal, Thermo Fisher Scientific) and washed with 170 µl CLIP wash buffer (1x PBS, 0.1% SDS, and 0.5% NP-40) twice for 10 minutes and then with 170 µl high salt wash buffer (5x PBS, 0.1% SDS, and 0.5% NP-40) twice for 10 minutes. The beads were then resuspended in RIPA buffer (25 mM Tris-Cl, pH 7.6, 150 mM NaCl, 1% NP-40, 1% sodium deoxycholate, and 0.1% SDS) and transferred to new tubes to remove nucleic acids attached to the tube walls. The crosslinks were reversed by incubating the beads with proteinase K at 37°C for 3 hours. The supernatant was collected as the RIP sample, and the RNA was extracted using TRIzol as described in the “Gene expression analysis” section. qPCR quantification was performed based on standard curves. The relative enrichment of the Srsf7 antibody was calculated by normalizing to the amount of RNA pulled down by the IgG control.

mRNA-seq

Cerebral cortex (CC) tissues were dissected from male mice at P1, P14 and P56 in triplicate. After homogenizing the tissues, total RNA was extracted with TRIzol (Invitrogen). To check the quality of the extracted RNA, the RNA integrity number (RIN) was determined using a Bioanalyzer (Agilent). The cDNA library was prepared using the TruSeq stranded mRNA library prep kit (Illumina). The quality of the cDNA library was checked with a Bioanalyzer and qPCR. The strand-specific sequencing was performed with HiSeq 2500 (read length: 50 base

pairs, single-end; Illumina) to generate Fastq files. The RNA-seq data were processed and analyzed using Bio-Linux 8 (Field et al., 2006). The triplicate data of cardiomyocytes and hepatocytes at P1, P7 and P56 were derived from our previously deposited dataset and are available at accession number DRA007101 in the DDBJ Sequence Read Archive (DRA).

To determine the juvenility-associated genes (JAGs) in the CC, the complete transcript set was filtered according to the following criteria: expression level higher than 0.5 fragments per kilobase of transcript per million fragments sequenced (FPKM) and fold change higher than 2 at both P1 and P14 compared to P56. Gene expression was visualized using Integrative Genomics Viewer (http://software.broadinstitute.org/software/igv/). Gene Ontology (GO) analysis was performed using the Database for Annotation, Visualization and Integrated Discovery (DAVID) v6.8 (https://david-d.ncifcrf.gov/).

Analysis of *Srsf7* heterozygous mutant tissues

Two *Srsf7* mutant mice and one WT littermate control were used. CC tissues were dissected from *Srsf7* mutant mice and a WT control littermate at P14. Cardiomyocytes and hepatocytes were isolated from *Srsf7* mutant mice and a WT control littermate as described previously (Jam et al., 2018). The total RNA extracted from the cells was processed as described above in *mRNA-seq*. The strand-specific sequencing was performed with a NovaSeq 6000 (read length: 100 base pairs, paired-end; Illumina) to generate Fastq files. The heatmaps were generated using MeV (http://mev.tm4.org).

Alternative splicing (AS) analysis

The AS patterns were comprehensively analyzed using MISO (Katz et al., 2010). Reads obtained from the high-throughput sequencing analyses were mapped to the reference genome (version mm10) using HISAT (Kim et al., 2015) to generate bam files. To determine the age-dependent alternative splicing (ADAS) events, MISO analysis was performed with the bam files of the CC, CMs and Heps at P1, P7 (for CMs and Heps) / P14 (for CC) and P56,

using “miso_annotations_mm10_v2” as the annotation. To determine the Srsf7-dependent AS events, MISO was used with the bam files of WT and *Srsf7* mutants as the input and “miso_annotations_mm10_v2” as the annotation. This procedure generated results for each AS type: “Exon skipping (ES)”, “Intron retention (IR)”, “Mutually exclusive exons (MXE)”, “Alternative 5’ splice sites (A5SS)” and “Alternative 3’ splice sites (A3SS)”. To count the AS events, splicing events with Bayes factors higher than $10^{1/2}$ were selected. For qPCR analysis, primers were designed to distinguish the juvenile and adult isoforms (sequences are shown in **Table S1**).

Phyre2 (http://www.sbg.bio.ic.ac.uk/phyre2/html/page.cgi?id=index, Kelley et al., 2015) was utilized to predict the secondary and tertiary structures of *Eif4a2* variants.

Minigene assay

For the minigene assays, mouse genomic sequences of *Eif4a2* (containing exon 10 to 12) and *Rbm7* (containing exon 1 to 3) were cloned into pcDNA3.1 vector. The WT control or the *Srsf7*-KO Neuro2a cells were transfected with each of the minigene plasmid and cultured for 72 hours. Total RNA was extracted and processed for the purpose of RT-PCR analysis. The primer pairs used for this experiment were shown in **Table S1**.

Statistical analysis

For all quantified data, mean ± standard deviation (SD) is presented. Statistical significance between two experimental groups is indicated by an asterisk and comparisons were made using the Student’s *t*-test. P-values less than 0.05 were considered significant.

Data and Code Availability

The accession numbers for the high throughput sequencing data reported in this paper are DNA Data Bank of Japan (DDBJ): DRA007101, DRA009510, DRA009537 and DRA009538.

Table S1. Sequence information. Related to Figures 2, 4, 6, 7, S3, S4 and S5.

The guide RNA-target sequence Species: Mouse

Srsf7	5'-GGCAATCCACACAGTTCTTAAGG-3'

Primers used for *Srsf7* genotyping

	Forward	Reverse
Srsf7 genotyping PCR and 1st round of nested PCR	5'-TGAGAGTCGTTTGAGCGATG-3'	5'-ACCACCGGAGCTATATGGTG-3'
2nd round of nested PCR	5'-ACGTGTACGTTGCACAGCTC-3'	5'-CCCACTTACTTCCCATCCAA-3'

Primers used for SYBR qPCR

Gene	Forward	Reverse
Srsf7	5'-ATTCGCCTTTGTGGAATTTG-3'	5'-GGTGGCCTATCAAAACGAGA-3'
Igf2	5'-GCCCTCCTGGAGACATACTG-3'	5'-ACGGGGTATCTGGGGAAGT-3'
Pdk1	5'-AAATGCGAAATCACCAGGAC-3'	5'-ACCTGAATCGGGGGATAAAC-3'
Pdk2	5'-AGCTGGTGCAGAGCTGGTAT-3'	5'-GACCAGGGCATCTGTGAACT-3'
Polr2a	5'-GAGTCCAGAACGAGTGCATGA-3'	5'-ACAGGCAACACTGTGACAATC-3'
Actb	5'-CTTTGCAGCTCCTTCGTTG-3'	5'-ACGATGGAGGGGAATACAGC-3'
Tubb5	5'-GATCGGTGCTAAGTTCTGGGA-3'	5'-AGGGACATACTTGCCACCTGT-3'
Eif4a2-juvenile form	5'-GGATTGACGTGCAACAAGTG-3'	5'-AATTACGTCAACGCCGTTTC-3'
Eif4a2-adult form	5'-GGATTGACGTGCAACAAGTG-3'	5'-CCCTCTGCCAATTCTGTGAA-3'
Rbm7-juvenile form	5'-TCCTCTTCGAGCTGTTCCAC-3'	5'-CCCAGCCTGTATGGTCAGAT-3'
Rbm7-adult form	5'-CTAGGCCTGGGACTGGAAC-3'	5'-TTACCGGCCCAGCCTGGTGG-3'

Primers used for cloning mouse *Eif4a2* and *Rbm7* for minigene constructs

	Forward	Reverse
*Eif4a2*_minigene_1,548bp	CGGGGATGTCTAGCTTTTTG	TAGGTCAGCCACATTCATGG
*Rbm7*_minigene_1,386bp	CCTTTACGTCGTGACGTCTG	AGCCAAAAACCCTCTCCCTA

Primers used for minigene assays

Gene	Forward	Reverse
Rbm7 minigene assay	5'-TTCTGAGGGTGCGCAGTAG-3'	5'-AGCAGATTCATGGCATAGGG-3'
Eif4a2 minigene assay	5'-TGCAACAAGTGTCCTTGGTTA-3'	5'-CCAATGCCTTTCCTCACAAG-3'

Primers used for RIP-qPCR

Gene	Forward	Reverse
Eif4a2	5'-TGACGAGATGGCACTCAGAA-3'	5'-CGACTCGCTCTTTATTCAAACA-3'
Rbm7	5'-TTGAGGCAGAGAGCCATATAGT-3'	5'-GAGATGCAGGCAGGAGGAC-3'
Rps13	5'-GTCCGAAAGCACCTTGAGAG-3'	5'-TTCCAATTAGGTGGGAGCAC-3'

Primers used for genome DNA quantification

Locus	Forward	Reverse
16S mitochondrial genome locus	5'-CCGCAAGGGAAAGATGAAAGAC-3'	5'-TCGTTTGGTTTCGGGGTTTC-3'
mt-Co1 mitochondrial genome locus	5'-GCCCCAGATATAGCATTCCC-3'	5'-GTTCATCCTGTTCCTGCTCC-3'
18S nuclear genome locus	5'-TAGAGGGACAAGTGGCGTTC-3'	5'-CGCTGAGCCAGTCAGTGT-3'